Large eddy simulation of fire-induced flows using Lattice-Boltzmann methods

Mostafa Taha, Song Zhao, Aymeric Lamorlette, Jean-Louis Consalvi, Pierre Boivin

Large eddy simulation of fire-induced flows using Lattice-Boltzmann methods

Mostafa Taha[a], Song Zhao[a], Aymeric Lamorlette[b], Jean-Louis Consalvi[b], Pierre Boivin[1a]

[a]*Aix Marseille Univ, CNRS, Centrale Marseille, M2P2, Marseille, France*
[b]*Aix Marseille Univ, CNRS, IUSTI, Marseille, France*

Abstract

Large-eddy simulations (LES) of the near-field region of large-scale fire plumes are performed for the first time with a pressure-based Lattice Boltzmann method (LBM) with low-Mach number approximation. Two scenarios are considered: the large-scale non-reactive helium plume and the 1 m methane pool fire, both investigated experimentally at Sandia. In the second scenario, a simplified modeling of the combustion and radiation processes is introduced involving a one-step irreversible reaction eddy-dissipation concept-based combustion model and a radiant fraction model, respectively. In both scenarios, a quantitative agreement is observed with the experimental data and model predictions are consistent with previously-published numerical studies. Our simulations demonstrate the computational efficiency of the proposed LBM solver to tackle fire-induced flows, suggesting that LBMs are a good alternative candidate for the modeling of fire-related problems.

Introduction

Computational Fluid Dynamics models play today an increasing role in fire safety engineering with the development of LES-based fire simulators such as FDS by the NIST and FireFoam by FM Global [1, 2]. The near field of well-controlled fire plumes offers a canonical scenario for the validation of such simulators since it involves most of the coupled physical processes encountered in fire problems, namely, buoyancy-controlled flows, buoyancy-

[1]Corresponding author: pierre.boivin@univ-amu.fr

induced turbulence, turbulent combustion, thermal radiation, soot generation, and, in the case of pool fires, burning rate [3].

LES of non-sooting and sooting fire plumes were reported in the literature with different levels of sophistication in the modeling of subrid-scale turbulence[4–14], turbulent combustion [14–16], radiative heat transfer [17–19], and soot modeling [16, 20, 21]. One of the difficulty in the modeling of the near field of fire plumes is that the flow, and the resulting air entrainment that controls the combustion process, is governed by the formation and growth of the flame base non-dissipative laminar instability near the edge of the pool that develops periodically to form energy containing large-scale toroidal vortices [22, 23]. A consequence is that these instabilities have to be spatially-resolved which requires a grid-resolution of the order of 2 mm [12–14].

The LES of fire plumes reported in the literature were performed by using classical Navier-Stokes solvers. On the other hand, Lattice Boltzmann Methods (LBM) appear as an attractive alternative to the classical Navier-Stokes solvers due to their lower computational cost, their capacities for massively parallel computing and the ease to deal with complex geometries using multi-level Cartesian grids [24]. These methods have been successfully applied to different classes of problems, including compressible flows [25–30], atmospheric flows [31–35], reactive flows [36–39] and, recently, to buoyancy-driven flows encountered in the far field of plumes [40].

The objective of this article is to explore for the first time the capacity of a pressure-based LBM solver with low-Mach number approximation [41] to handle fire-related flows. An hybrid strategy is considered where continuity and momentum are solved with the LBM equation and transport equations for other scalars (enthalpy, chemical species,...) are solved by classical finite difference methods. The numerical model is applied to provide LES of two scenarios representative of unwanted fires. The first involves the large-scale helium plume investigated at Sandia [42, 43]. The main advantage of this configuration is that it mimics the dynamics and structure of large-scale fire plumes while avoiding the complexities associated with combustion and radiation. The second configuration is relative to the 1 m methane fire plumes also investigated at Sandia [44, 45]. This scenario enhances the complexity of the first as it involves turbulent combustion and thermal radiation.

The article is organized as follows. A detailed description of the experimental setup is first given. Section 2 presents the numerical method,

including the LBM strategy, the different turbulence, combustion and radiation models. The results for the helium plume scenario and the methane pool fire are presented in Sections 3 and 4, respectively. Conclusions are finally drawn to highlight the findings of this study and suggestions for future work.

1. Experimental setup

Comparisons are made in this study with experiments performed in the Fire Laboratory for Accreditation of Models and Experiments (FLAME) at Sandia National Laboratories in Albuquerque, New Mexico [42]. The considered experiments involve either a non-reactive helium plume scenario or a reactive scenario with methane as fuel. The central FLAME chamber consists of a 6.1 m cubical enclosure with a 2.4 m diameter chimney.

The plume source is 1 m in diameter surrounded by a 0.51 m wide floor (i.e. the ground plane). Further details about the facility can be found in Tieszen et al. [42].

For the non-reactive case, a gas mixture, composed of 96.4% helium, 1.7% acetone, and 1.9% oxygen by volume, with a molecular weight of 5.45 g/mol, was injected at an average velocity of 0.325 m/s. Measurements were obtained using particle image velocimetry (PIV) for velocity field measurements and planar laser-induced fluorescence (PLIF) for helium mass fraction [43]. The experimental uncertainty on the measured velocities, concentrations, turbulent statistics, and concentration fluctuations is estimated to be around ± 20, ± 18, ± 30, and $\pm 21\%$, respectively.

For the methane pool fires, Tieszen *et* al. [44, 45] measured the velocity field for methane fire plumes with different heat release rates ranging from 1.56 to 2.61 MW. Nonetheless, no measurements for temperature were performed. Numerous tests were conducted during the experimental study [44, 45] where the fuel inlet conditions were varied to cover a wide range of fire regimes. TEST-24 is chosen as a reference for our numerical study and whose inlet and boundary conditions are summarized in Tab. 1.

2. Lattice-Boltzmann model for Low-Mach flows

2.1. Macroscopic governing equations

The leading order flow mass, momentum, and energy conservation equations are introduced as [41]:

Fuel	CH_4
Fuel inlet velocity (m/s)	$0.097 \pm 3\%$
Fuel mass flux (kg/m^{2}s)	$0.053 \pm 3\%$
Heat release rate (MW)	$2.07 \pm 8\%$
Ambient pressure (kPa)	81.0 ± 0.2
Ambient temperature (K)	290 ± 3

Table 1: Initial and boundary conditions of TEST-24 in the experiments [44, 45]

$$\frac{\partial \rho}{\partial t} + \frac{\partial \rho u_i}{\partial x_i} = 0 \tag{1}$$

$$\frac{\partial \rho u_i}{\partial t} + \frac{\partial (\rho u_i u_j + \delta_{ij} p^h)}{\partial x_j} = \frac{\partial \Pi_{ij}}{\partial x_j} + (\rho - \rho_\infty) g_i, \qquad (i = 1, 2, 3) \tag{2}$$

$$\nabla P = 0 \tag{3}$$

$$\rho \frac{\partial h}{\partial t} + \rho u_i \frac{\partial h}{\partial x_i} = \frac{dP}{dt} - \frac{\partial q_i}{\partial x_i} + \Pi_{ij} \frac{\partial u_i}{\partial x_j}, \tag{4}$$

$$\rho \frac{\partial Y_k}{\partial t} + \rho u_i \frac{\partial Y_k}{\partial x_i} = \frac{\partial}{\partial x_i} (\rho Y_k V_{k,i}) + \dot{\omega}_k, \tag{5}$$

where ρ is the density, u_i is the velocity vector, p^h is the hydrodynamic pressure, P is the thermodynamic pressure, g_i is the gravitational acceleration, δ_{ij} as the Kronecker delta symbol, ρ_∞ is the ambient density. The viscous stress tensor Π_{ij} in Eqs. (2-4) reads:

$$\Pi_{ij} = \mu \left(\frac{\partial u_i}{\partial x_j} + \frac{\partial u_j}{\partial x_i} - \delta_{ij} \frac{2}{3} \frac{\partial u_k}{\partial x_k} \right), \tag{6}$$

with μ the dynamic viscosity. In enthalpy equation (Eqn. 4), h represents the mass enthalpy. Throughout this work, we set the temporal variation of the thermodynamic pressure to zero, i.e., $dP/dt = 0$, to meet the open boundary conditions [41, 46]. The heat flux q_i in the enthalpy equation reads:

$$q_i = -\lambda \frac{\partial T}{\partial x_i} + \sum_{k=1}^{N_{sp}} \rho h_k Y_k V_{k,i}, \tag{7}$$

where T is the temperature, λ the heat conductivity, obtained assuming constant Prandtl number (Pr):

$$\mathrm{Pr} = \frac{c_p \mu}{\lambda}. \tag{8}$$

h_k is the partial enthalpy of species k, Y_k is its mass fraction, and $V_{k,i}$ is its diffusion velocity vector. The term $Y_k V_{k,i}$ constitutes the species mass flux. The species mass flux is modeled by *Hirschfelder and Curtiss* approximation equipped with a correction term ensuring global mass conservation:

$$Y_k V_{k,i} = -\mathcal{D}_k \frac{\mathcal{W}_k}{\mathcal{W}} \frac{\partial X_k}{\partial x_i} + V_i^c Y_k, \tag{9}$$

where $\mathcal{D}_k$ is the molecular diffusion coefficient of species k, $\mathcal{W}_k$ is its molecular weight and X_k is its molar fraction. $\mathcal{W}$ is the average molecular weight and V_α^c the correction velocity introduced in order to ensure the conservation of total mass (i.e., ensuring $\sum_{k=1}^{N_{sp}} Y_k V_{k,\alpha} = 0$) which can be evaluated by:

$$V_\alpha^c = \sum_{k=1}^{N_{sp}} \mathcal{D}_k \frac{\mathcal{W}_k}{\mathcal{W}} \frac{\partial X_k}{\partial x_\alpha}. \tag{10}$$

$\mathcal{D}_k$ is linked to the viscosity through Schmidt number (Sc) as:

$$\mathrm{Sc} = \frac{\mu}{\rho \mathcal{D}_k}. \tag{11}$$

The system of Eqs (1-5) is fully closed by the choice of an equation of state:

$$P = \rho.r.T \ , \qquad h = \sum_{k=1}^{N_{sp}} h_k Y_k = \sum_{k=1}^{N_{sp}} Y_k \left(\int_{T_0}^{T} c_{p,k}(\theta) d\theta + \Delta h_k^0 \right) \tag{12}$$

with P the thermodynamic pressure, $c_{p,k}$ and Δh_k^0 the constant pressure heat capacity and the formation enthalpy of species k respectively, and $r = \mathcal{R}/\mathcal{W}$ the gas constant where $\mathcal{R} = 8.314 \mathrm{J\,K^{-1}}$ is the universal gas constant and its molecular weight is $\mathcal{W}$.

2.2. Turbulence modeling

The filtered expressions for Eqs. 1-5 are widely reported in the literature (see, e.g., Ref. [46]) and not recalled here. Subgrid-scale models (i.e. turbulence models) are essential to estimate the subgrid terms appearing in the filtered equations. Applying the subgrid-scale model numerically comes down to modifying the viscosity μ through the addition of a turbulent viscosity μ_t. Turbulent models aimed to estimate the correct value of μ_t that compensate the non-resolved structures filtered by the mesh (i.e. smaller than the mesh size).

2.2.1. Smagorinsky model

The first model to be introduced is the Smagorinsky model [47]. It is constructed of a length scale term, a time scale length, and a dimensionless constant C_s called Smagorinsky constant. The turbulent viscosity μ_t is calculated through:

$$\mu_t = \rho(C_s\Delta_m)\left|\widetilde{S}\right|, \tag{13}$$

where Δ_m is the local mesh size, and $\left|\widetilde{S}\right|$ is the filtered rate of stress tensor written as:

$$\left|\widetilde{S}\right| = \sqrt{2\widetilde{S_{ij}}\widetilde{S_{ij}}}, \tag{14}$$

with $\widetilde{S_{ij}}$ reads:

$$\widetilde{S_{ij}} = \frac{1}{2}(\frac{\partial\widetilde{u_i}}{\partial x_j} + \frac{\partial\widetilde{u_j}}{\partial x_i}), \tag{15}$$

Care should be taken when using the Smagorinsky model because it has many drawbacks listed below:

- C_s is a predefined input to the simulation, this constant can not represent correctly various turbulent flows.
- The eddy viscosity does not vanish for laminar flows.
- The back-scatter of energy from small scale to large scale is prevented completely since:
$$(C_s\Delta_m^2)\sqrt{2S_{ij}S_{ij}} \geq 0 \tag{16}$$
- Smagorinsky model introduces too much diffusion to the flow.

2.2.2. Vreman model

Inspired from the Smagorinsky model, Vreman subgrid model was introduced [48], where the μ_t is described as:

$$\mu_t = \rho C\sqrt{\frac{B_\beta}{\alpha_{ij}\alpha_{ij}}}, \tag{17}$$

with,

$$\alpha_{ij} = \frac{\partial u_j}{\partial x_i}, \tag{18}$$

$$\beta_{ij} = \Delta_m^2\alpha_{mi}\alpha_{mj}, \tag{19}$$

$$B_\beta = \beta_{11}\beta_{22} - \beta_{12}^2 + \beta_{11}\beta_{33} - \beta_{13}^2 + \beta_{22}\beta_{33} - \beta_{23}^2, \tag{20}$$

The constant C is related to the Smagorinsky constant C_s as $C = 2.5C_s^2$. Vreman model was developed in a try to fix the downsides of Smagorinsky model. Both Smagorinsky and Vreman models are simple to implement as they only require the local filter width (i.e. mesh size) and the first order derivatives of the velocity field.

2.3. Combustion modeling

The combustion modeling aims to compute the species production term $\dot{\omega}_k$ (i.e. combustion source term) in the species conservation equation (Eqn. 5). The eddy dissipation concept (EDC), which is commonly incorporated in fire simulators such as FDS [49] and FireFoam [2], is adopted in the present study [50]:

$$\dot{\omega}_F = C_{\mathrm{EDC}}\overline{\rho}\frac{1}{\tau_t}\min\left(\widetilde{Y_F}, \frac{\widetilde{Y_O}}{s}\right) \tag{21}$$

where $\dot{\omega}_F$ is the fuel mass consumption rate per unit volume (i.e. Kg m^{-3} s^{-1}), C_{EDC} is the model constant, $\overline{\rho}$ is the averaged density, τ_t is the turbulent/mixing time scale, $\widetilde{Y_F}$ and $\widetilde{Y_F}$ are the filtered mass fraction of fuel and oxidizer respectively and finally s is the stoichiometric oxygen-to-fuel mass ratio. The main parameter that controls and defines the dynamics of the EDC model is the turbulent/mixing time scale τ_t. Following the work of Yaga *et* al. [51], the C_{EDC} is set to 4.0 whereas the eddy characteristic time τ_t is estimated by considering the Kolomogorov scale as:

$$\tau_t = \left(\frac{\nu}{\epsilon}\right)^{\frac{1}{2}}, \tag{22}$$

where ϵ is the dissipation rate of turbulent kinetic energy and ν is the kinematic molecular viscosity. Assuming local equilibrium between production and dissipation of turbulent kinetic energy (same hypothesis adopted while deriving Smagorinsky SGS model), eddy dissipation rate ϵ is written as follows:

$$\epsilon = 2\nu_t\widetilde{S_{ij}} : \widetilde{S_{ij}}, \tag{23}$$

where ν_t is kinematic turbulent viscosity and $\widetilde{S_{ij}}$ is the strain rate, both described in Sec. 2.2. The eddy characteristic time scale will then be:

$$\tau_t = \left(\frac{\nu}{2\nu_t\widetilde{S_{ij}} : \widetilde{S_{ij}}}\right)^{\frac{1}{2}}. \tag{24}$$

Note the term $\widetilde{S_{ij}} : \widetilde{S_{ij}}$ is an inner product and should calculated as follows:

$$\widetilde{S_{ij}} : \widetilde{S_{ij}} = \widetilde{S_{11}}^2 + \widetilde{S_{22}}^2 + \widetilde{S_{33}}^2 + 2\left(\widetilde{S_{12}}^2 + \widetilde{S_{13}}^2 + \widetilde{S_{23}}^2\right). \tag{25}$$

A simple radiant fraction-based model is introduced to account for radiative loss. In this approach, commonly used in fire simulators [1], a specified part of the local heat release rate is assumed to be lost by radiation [1, 2].

2.4. LBM description for Low-Mach number approximation

For a complete description of the numerical method, the reader is referred to Farag et al. [28, 29]. Lattice-Boltzmann methods are derived from a space, time, and velocity discretization of the Boltzmann equation [52]. In the present model, the probability density function f_i is solved at each point x via the Boltzmann equation discretized as:

$$f_i\left(x + c_i\delta t, t + \delta t\right) = f_i^{\mathrm{eq}}\left(x,t\right) + \left(1 - \frac{\delta t}{\tau}\right) f_i^{\mathrm{neq}}\left(x,t\right) + \frac{\delta t}{2} F_i^E(x,t) \tag{26}$$

where δt is the time-step, and c_i is the i^{th} discrete velocity of the D3Q19 lattice[24], and F_i^E is a volume force including gravity and correcting terms, as defined in Appendix A. The equilibrium and off-equilibrium populations $(f_i^{\mathrm{eq}}, f_i^{\mathrm{neq}})$ are to be defined in Eqs (28, 29).

In Eq. (26), the relaxation time τ is related to the dynamic viscosity as:

$$\tau = \frac{\mu}{\rho c_s^2} + \frac{\delta t}{2}, \tag{27}$$

where $c_s = \delta x/(\sqrt{3}\delta t)$ is the characteristic velocity of the D3Q19 lattice [24].

The equilibrium function is obtained as

$$f_i^{\mathrm{eq}} = \omega_i \left(\rho\theta + \frac{\mathcal{H}_{i,\alpha}^{(1)}}{c_s^2}\rho u_\alpha + \frac{\mathcal{H}_{i,\alpha\beta}^{(2)}}{2c_s^4}\rho u_\alpha u_\beta + a^{(3)} + a^{(4)}\right), \tag{28}$$

where ω_i is the D3Q19 weight of discrete velocity c_i, $\mathcal{H}_i$ are the discrete Hermite polynomials, defined in Appendix A, and $a^{(3)}$ and $a^{(4)}$ are third and forth order terms also provided in Appendix A.

The off-equilibrium counterpart f^{neq} is obtained as:

$$f_i^{\mathrm{neq}} = \omega_i \left[\frac{\mathcal{H}_{i,\alpha\beta}^{(2)}}{2c_s^4} a_{\alpha\beta}^{(2),\mathrm{neq}} + \frac{\mathcal{H}_{i,\gamma}^{(3r)}}{6c_s^6} a_{\gamma}^{(3r),\mathrm{neq}}\right], \tag{29}$$

with

$$a_{\alpha\beta}^{(2),\mathrm{neq}} \equiv a_{\alpha\beta}^{*(2),\mathrm{neq}} - \frac{\delta_{\alpha\beta}}{3} a_{\gamma\gamma}^{*(2),\mathrm{neq}}, \tag{30}$$

$$a_{\alpha\beta}^{*(2),\mathrm{neq}} = \sum_i \left[\left(f_i - f_i^{\mathrm{eq}} + \frac{\delta t}{2} F_i^E \right) \mathcal{H}_{i,\alpha\beta}^{(2)} \right]. \tag{31}$$

and the third-order contribution defined in Appendix A.

Following the work introduced recently by Wang *et al.* [41], the compressible description of LBM can be adjusted to follow the low-Mach number approximation (LMNA). This approach divides the pressure field into the thermodynamic part, p^{th}, and the hydrodynamic part, P. The thermodynamic pressure is linked to the equation of state and is spatial independent. Thus, only the hydrodynamic pressure appears in the momentum conservation equation. In practice, the density field is updated using the thermodynamic pressure and the temperature field, i.e.

$$\rho(x, t+\delta t) = \frac{P(t+\delta t)}{rT(x, t+\delta t)}. \tag{32}$$

For the simulations in this paper, the thermodynamic pressure P is assumed to be constant, considering the open boundary conditions.

The hydrodynamic pressure cooperates with the LBM system through the reduced temperature

$$\theta \equiv \frac{p^h}{\rho c_s^2}\ , \tag{33}$$

and p^h will be updated following

$$p^h(x, t+\delta t) = p^h(x,t) + c_s^2 \left[\sum_i \left\{ f_i^{col}(x - c_i \delta t, t) - f_i^{col}(x,t) \right\} - (\rho(x, t+\delta t) - \rho(x,t)) \right]. \tag{34}$$

The velocity fields are calculated through the first-order moment of the LBM population

$$\rho u_i(x, t+\delta t) = \sum_i c_i \left(f_i(x, t+\delta t) + \frac{\delta t}{2} F_i^g \right), \tag{35}$$

where F_i^g is the gravity force term defined in Appendix A.

The enthalpy equation (4) is solved at the same time using a finite difference discretization under the non-conservative form, exactly as presented

by Tayyab *et al.* [36, 37]. Second-order consistency to the macroscopic equations (1-4) can be shown via Chapman-Enskog [52], or Taylor [53, 54] expansions.

3. Sandia's 1-m diameter helium plume

3.1. Numerical setup

The simulation is performed on a Cartesian mesh for a cubic domain sizing $8 \times 8 \times 4\,\mathrm{m}^3$ depicted in Fig. 1. The choice of the domain size as well as the grid resolution is consistent with previous numerical studies [4, 7, 55, 56].

Three meshes were included in our study, and refinements zones were used to reduce the calculation cost. The zones of refinements (Fig. 1) are denoted by *ZoneI*, *ZoneII*, *ZoneIII* and *ZoneIV* with grid size reduced in half between two adjacent zones. The coarse mesh contains *ZoneI*, *ZoneII* and *ZoneIII* corresponding to grid size of 8 cm, 4 cm and 2 cm, respectively, resulting in a 2 million-cell mesh. This coarse grid will be referred to as $\Delta x = 2$ cm hereafter. In the medium and fine meshes, an additional refinement zone is added close to the plume source, indicated by *ZoneVI* in Fig. 1, to end up with four levels of refinements. For the medium grid, the largest and smallest grid size are of 8 cm and 1 cm, respectively, resulting in a 4 million-cell mesh. This medium grid will be referred to as $\Delta x = 1$ cm hereafter. For the fine, the mesh sizes are deduced from the medium grid by applying a scaling factor of 0.8 in each zone. A consequence is that the the largest and smallest grid size are of 6.4cm and 0.8 cm, respectively, resulting in a 7.8 million-cell mesh. This fine grid will be referred to as $\Delta x = 0.8$ cm hereafter.

Boundary conditions are given in Fig. 1. Helium is injected at the center of the bottom plane through a 1 m diameter inlet with a uniform vertical velocity $U^{He}_{inlet} = 0.325\,\mathrm{m/s}$. The helium inlet is surrounded by an annulus solid plate of 0.5 m width beyond which a co-flow of air is injected at a much lower speed $U^{Air}_{coflow} = 0.01\,\mathrm{m/s}$. At the upper outlet plane a Dirichlet boundary condition is used for pressure and Neumann for other variables, with a clip on the streamwise velocity to prevent any backflow from the outlet. The sides are set to a typical In/Out flow.

At every point in the domain, the composition of the fluid corresponds to a mixture of helium and air. The air was treated as a whole specie without separating Oxygen and Nitrogen with an average molecular weight of the air is taken $W_{air} = 28.9\mathrm{g\,mol}^{-1}$. For experimental visualization reasons, the

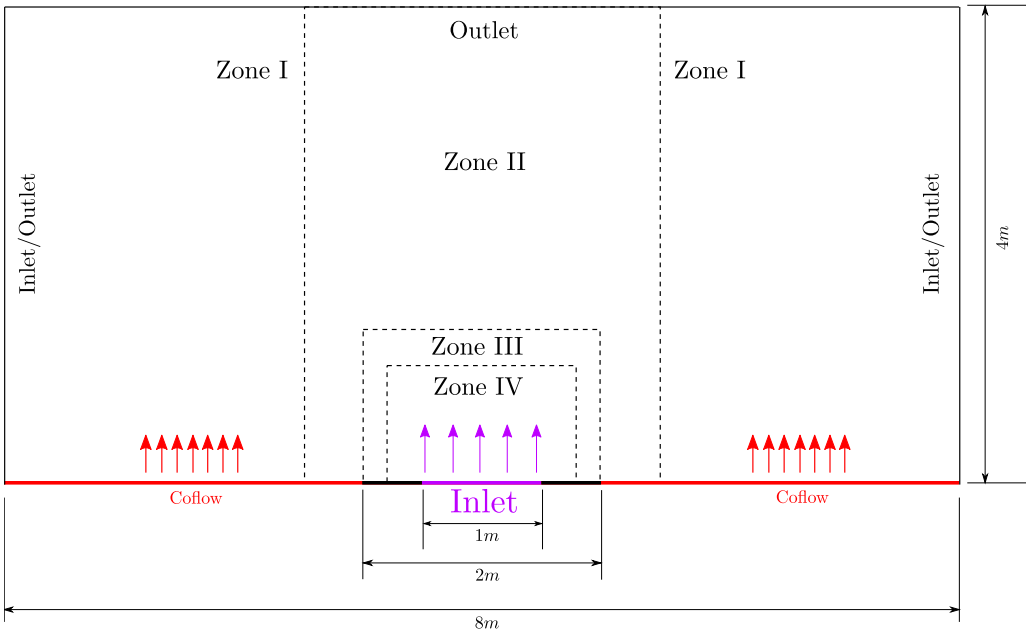

Figure 1: Schematic of the computational domain including refinement zones and boundary conditions.

injected helium was not pure, but rather a mixture of 96.4% helium (He), 1.9% oxygen (O_2) and 1.7% acetone (CH_3COCH_3) resulting in an average molecular weight $W_{He} = 5.45\text{g}\,\text{mol}^{-1}$. The ambient (also inlet) temperature and pressure are $T_\infty = 285\,\text{K}$ and $p_\infty = 80900\text{Pa}$, respectively, in order to match the experimental setup.

The Prandtl number Pr was set to 0.7 while the Schmidt number of helium Sc_{He} is set to 0.2. The dynamic viscosity μ has a constant value of $1.8877 \times 10^{-5}\,\text{kg}\,\text{m}^{-1}\,\text{s}^{-1}$ for both air and helium. Resulting in a Reynolds number $\text{Re} \simeq 3220$ and a Richardson number $\text{Ri} \simeq 75.4$, matching the experiment.

In the case of homogeneous isotropic turbulence, the model constant is estimated as $C_s = 0.2$ [46]. However, C_s depends on the flow configuration with values of $C_s \approx 0.1 - 0.2$ often used [57]. For this simulation, the Smagorinsky model is used (Sec. 2.2) with a constant $C_s = 0.1$ as suggested by Maragkos *et* al. [8].

The un-resolved SGS heat and species diffusion fluxes are estimated using the turbulent Prandtl Pr_t and the turbulent Schmidt Sc_t, respectively. Both are set to 0.5 as Maragkos et al. [8] and Chung et al. [55].

The large-eddy simulation is run for 26 s of physical time. The first 13 s are to ensure the evacuation of the initial field and to reach statistically stationary flow conditions, and the other 13 s are used to construct the mean and RMS quantities of the plume. The simulations are performed at a constant CFL number equaling to 0.6 such that the time step would depend on the local mesh size. The CFL number is defined as:

$$\text{CFL}_u = \frac{(u + c_{black})\delta t}{\delta x} \tag{36}$$

where c_{black} denotes the fictitious reduced speed of sound following the low-Mach number approximation. The time-step is local (it is halved/doubled at each mesh transition), and is $\delta t = 38\,\mu\text{s}$ on the smallest mesh region (where $\Delta x = 0.8\text{cm}$). In other words, the CFL number (36) is kept almost constant in the whole domain. The simulations are parallelized on 120 cores on a Dell PowerEdge C6420 server with 4× 32-core Intel Xeon Gold 6142, 2.6 GHz, and 96 GB RAM. The computational cost of the simulation with the finest mesh is compared to other studies in Table 2. The corresponding reduced computational time (cost per iteration per grid point) is close to 2.4µs, an excellent score when comparing with available computational benchmarks [58–60]. Another advantage of the present approach is that complex geometry can be easily tackled at no extra cost [61]. Finally,

the considered Lattice-Boltzmann regularized kernel is well suited for cross-platform cpu-gpu usage [62], allowing to envision significant speedups in the future.

Reference	mesh	δx_{min}	t_{total}	CPU hours / 1 sec	CPU hours / 1 sec / 1M cell
DesJardin et al. [4]	2.5M	1.6 cm	20 sec	700	280
Maragkos et al. [8]	1.26M	1.23 cm	30 sec	78	62
Current study	7.8M	0.8 cm	26 sec	130	16

Table 2: Cost comparison between different numerical studies for the finest mesh.

3.2. Results and discussions

3.2.1. Turbulence

Figure 2 shows the energy spectrum based on the axial velocity at distance $z = 0.5\ m$. The $-5/3$ power law, predicted by the the theory of Kolmogorov [63], is well reproduced.

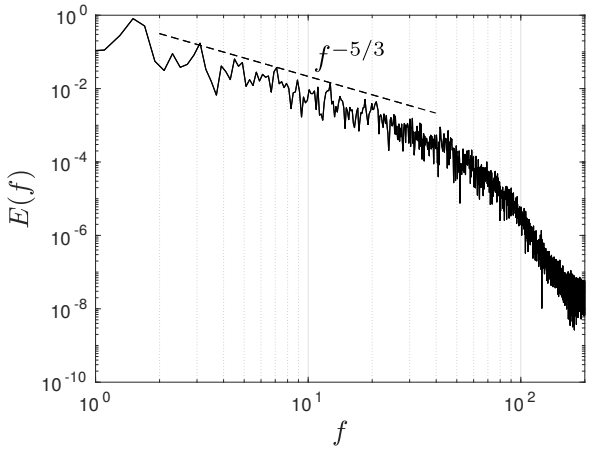

Figure 2: Temporal energy spectrum at $z = 0.5\ m$ for axial velocity. Dashed line indicate the expected characteristic slope of $-5/3$ [63].

3.2.2. Instability modes and vortex dynamics

Figure 3 shows a typical puffing cycle. A puffing cycle can be divided into four distinct phases: In the first phase, instabilities form near the edge of the plume as observed in Fig. 3(a). The trigger of these instabilities is

the misalignment of pressure and density gradients which generates a localized torque (baroclinic torque). Those instabilities grow and entrain large quantity of the surrounding fluid, forming into a toroidal vortex as shown in Fig. 3(b). While this vortex moves upwards more fluid is pumped at the center of the plume causing a large streamwise velocity at the centerline as shown in Fig. 3(c). The increase in streamwise velocity at the centerline causes a sharp increase in cross-stream velocity near the base of the plume, as a result of mass conservation, providing a perturbation of the mixing layer for the next cycle (Fig. 3(d)).

Strong instabilities are observed at the helium-air interface near the plume source, and it is important to capture those small dynamics as discussed in the introduction [12–14]. These instabilities are generated by buoyancy-driven (gravitational and baroclinic) vorticity generation. Thus, Rayleigh-Taylor and Kelvin-Helmholtz instabilities are triggered, near the base of the plume, and at last they will form the toroidal structures [4, 43] as shown in Fig. 3(d).

A better understanding can be made from the analysis of the vorticity equation:

$$\frac{D\boldsymbol{\omega}}{Dt} = \underbrace{(\boldsymbol{\omega}\cdot\nabla)\mathbf{u}}_{\text{vortex stretching}} - \underbrace{\boldsymbol{\omega}(\nabla\cdot\mathbf{u})}_{\text{dilatation term}} + \underbrace{\frac{1}{\rho^2}(\nabla\rho\times\nabla p)}_{\text{baroclinic torque}} + \underbrace{\frac{\rho_\infty}{\rho^2}(\nabla\rho\times g)}_{\text{gravitational torque}} + \underbrace{\nabla\times(\frac{1}{\rho}\nabla\cdot\tau)}_{\text{viscous diffusion}} \tag{37}$$

On the right hand side of Eq. (37), five different physical mechanisms affect the vorticity transport. Those five terms are identified as vortex stretching, dilatation term, baroclinic torque, gravitational torque and viscous diffusion [64]. In incompressible flows, only the first term prevails. Vortex stretching represents the enhancement of vorticity by stretching, it is an essential mechanism by which turbulent energy is transferred to smaller scales. The dilatation term represents the effects of vorticity field expansion which causes a decrease in vorticity magnitude. Gravitational torque generates vorticity due to the misalignment of gravity and density gradients, while baroclinic torque generates vorticity as a result of non-aligned pressure and density gradients. In buoyancy-driven flows, both the baroclinic and gravitational torque terms are the principal mechanisms generating flow vorticity [64, 65]. The DNS [66] demonstrated that the gravitational

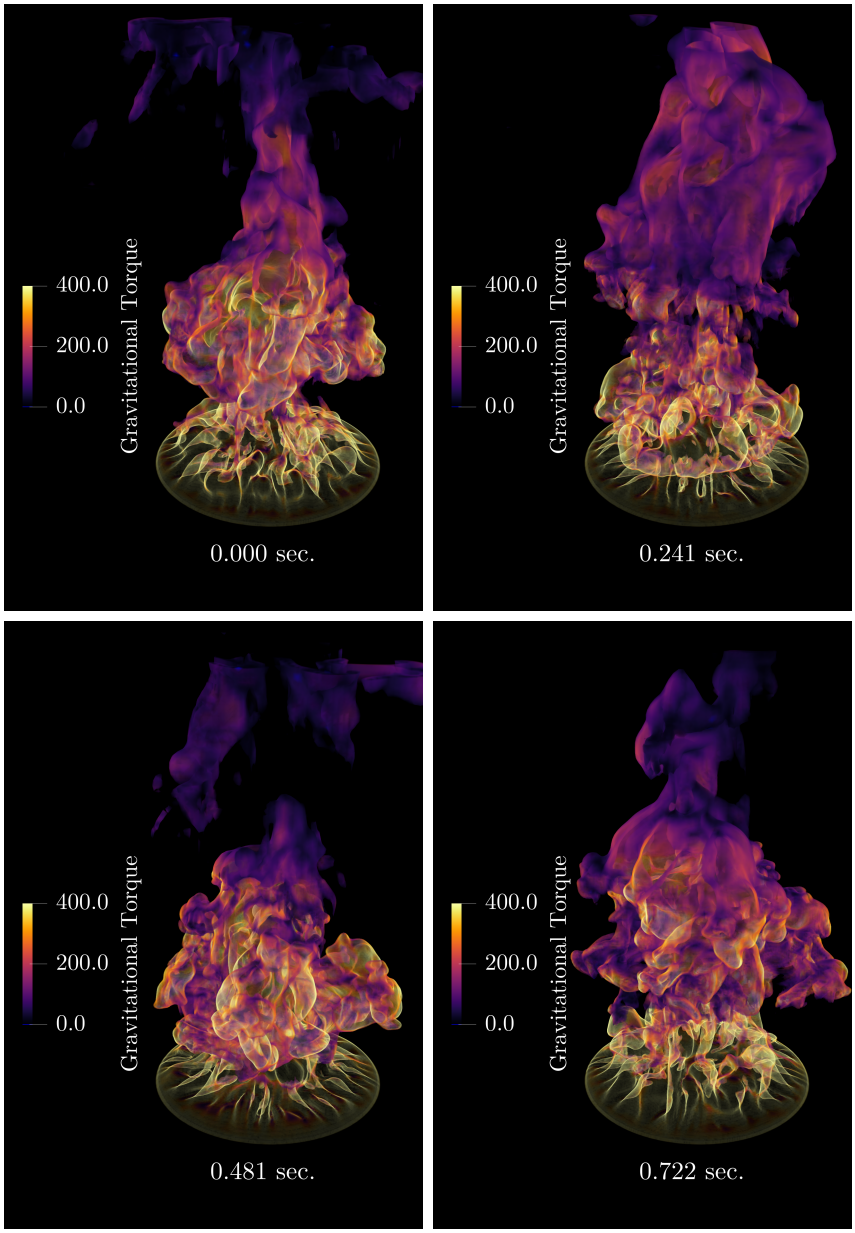

Figure 3: Instantaneous iso-volume of density colored by gravitational torque magnitude showing a complete puffing cycle. From left to right 4 different instances were captured which extend over around 0.7 sec which is the periodic time of a puffing cycle.

torque is fundamental mechanism promoting cross-stream vorticity. LES studies [4, 8] observed that during typical puffing cycle, the maximum grav-

itational torque is located at the base of the plume. The same behavior can be observed in the current study, as seen in Fig. 3 where the maximum value of gravitational torque is observed at the base of the plume. The contribution of the baroclinic torque has similar importance. Maximum values can be located in zones where large pressure and density gradients exist near the base of the plume. Both torques trigger the instabilities at the base and then nurture its growth. For large plumes and pool fires, this vortex destabilizes rapidly forming secondary azimuthal, or "finger-like" instabilities that can be detected in Fig. 3, which were also observed experimentally [22, 67]. Those secondary instabilities create streamwise vorticity that promote the breakdown of large scale toroidal structures and improves the local mixing eventually. Capturing these instabilities and mechanisms is therefore a prerequisite for pool fire simulation because the combustion process for this type of flows is controlled mainly by the mixing process of fuel and oxidizer.

3.2.3. Puffing frequency

Figure 4 shows both the temporal signal of the centerline streamwise velocity at $z = 0.5\,\mathrm{m}$ and the corresponding power density spectrum obtained from Fast Fourier transform (FFT). The signal extends over 5 s of physical time, from 13 to 18 s, in order to be compared with the experimental one. It is worth mentioning that results revealed a small phase shift compared to the experiment, probably because we do not have the exact same initialization as in the experiment. Thus, the simulation time signals in Fig. 4 have been shifted along the time axis to match the first peak of the experimental signal for the sake of clearer comparison.

Around 9 cycles are identified for the coarse mesh and 7 cycles for both medium and fine meshes, versus 7 cycles found in the experiment [43]. In addition, the predicted puffing frequency is 1.69 Hz for the coarse grid and 1.39 Hz for both the medium and fine grids whereas the observed experimental frequency was $1.37 \pm 0.1\,\mathrm{Hz}$. These results suggest that a converged solution is obtained for the medium grid. This will be further demonstrated when discussing the profiles of velocities and helium mass fraction. The predicted puffing frequency on both the medium and fine meshes is also consistent with the experimental correlation proposed by Cetegen and Kasper [68] $f = 0.8\mathrm{Ri}^{0.38}U_p/D_p = 1.34\,\mathrm{Hz}$ from measurements of helium-air plumes for $\mathrm{Ri} < 100$. In this expression, Ri is a modified Richardson number defined as $\mathrm{Ri}_1 = (\rho_\infty - \rho)gD_p/(\rho_\infty U_p^2) \simeq 76$. Furthermore, the results are also inline with the experimental correlation given by Cetegen and Ahmed [22] for buoyant diffusion flames (i.e. pool fire) of various fuels

$f = 1.5/\sqrt{D_p} = 1.5\,\text{Hz}$. The disparity from this latter correlation may be attributed to the fact that it was suggested for diffusion flames. These results highlight that the finer mesh enables the correct prediction of the instabilities generated near the inlet which is the main trigger of the puffing motion. The same conclusion was drawn by Maragkos *et* al. [8], DesJardin *et* al. [4] and Ma *et* al. [56].

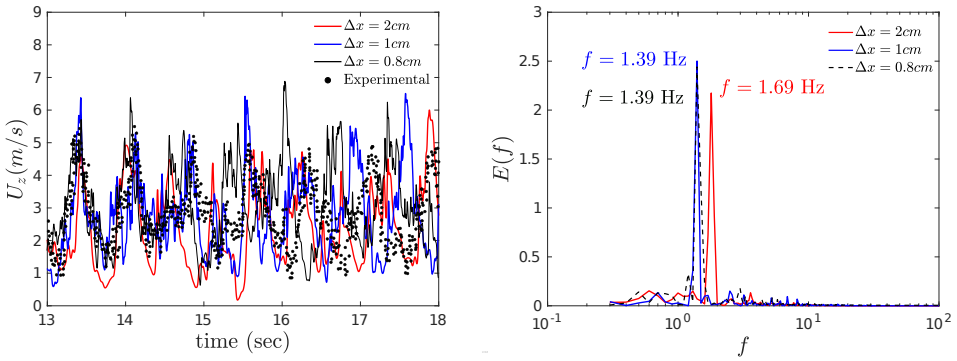

Figure 4: (left) Time series of centerline streamwise velocity at $z/D = 0.5$ in a window of 5 s. (right) Power spectrum of the centerline streamwise velocity U_z. The principle frequency (i.e. puffing frequency) is indicated on the figure. The sampling time ts to construct the power spectrum is taken to be each 10 time steps that is $ts_{coarse} = 9.6 \times 10^{-4}$ sec, $ts_{medium} = 4.8 \times 10^{-4}$ sec and $ts_{fine} = 3.8 \times 10^{-4}$ sec for the coarse, medium and fine mesh, respectively.

3.2.4. Statistics of velocity and mass fraction

The mean values and high order statistics (i.e. rms) are discussed in this section. In all the figures the data with bars represents the experimental results of O'Hern *et* al. [43] including the experimental uncertainties as explained in Sec. 1. Furthermore, we added the results of the LES presented by Marakgos *et* al. [8], DesJardin *et* al. [4] and Ma *et* al. [56] for further comparisons.

Figure 5 shows the centerline mean and rms profiles of the streamwise velocity up to $z = 0.8$ m above the helium source. Both profiles predicted by the medium ($\Delta x = 1$ cm) and fine ($\Delta x = 0.8$ cm) grids are in close agreement and within the experimental uncertainties at all locations along the plume axis. The rms are more difficult to predict which is consistent with the findings of Maragkos *et* al. [8].

The mean and rms profiles of helium mass fraction along the centerline up to a height of $z = 0.8$ m are displayed in Fig. 6. The mean Y_{He}

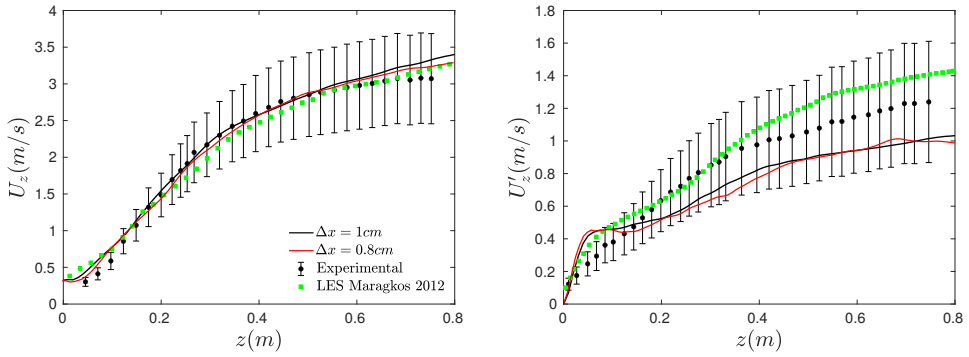

Figure 5: Comparison of mean (left) and rms (right) of centerline streamwise velocity. The experimental data includes the respective uncertainties reported in the experimental study [43]. The numerical results of Maragkos *et* al. [8] are also added.

profile follows that predicted by Maragkos *et* al. [8] and decays in a slower manner as compared to the experiment beyond $z = 0.3\,\mathrm{m}$. Consistently with the results of Marakgos *et* al. [8], the rms Y'_{He} profile is significantly over-predicted over the entire axis. It can be observed that the predictions obtained with both the medium ($\Delta x = 1$ cm) and fine ($\Delta x = 0.8$ cm) grids are very similar, confirming that converged solutions are obtained with the medium grid. Hereafter, only the results obtained with medium grid will be shown.

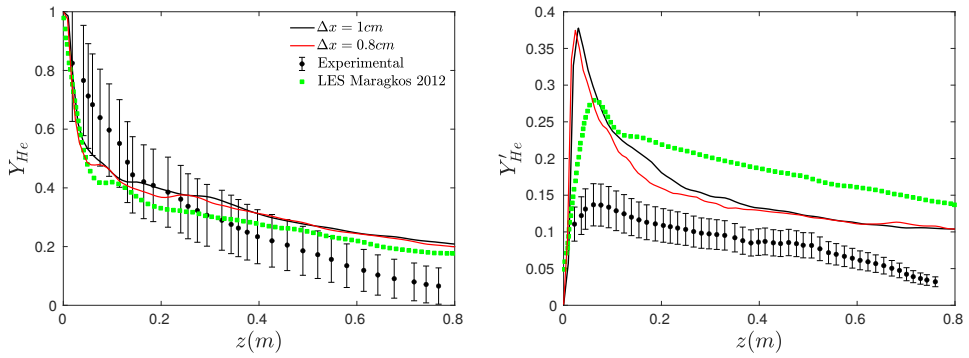

Figure 6: Comparison of mean (left) and rms (right) of centerline helium mass fraction. The experimental data includes the respective uncertainties reported in the experimental study [43]. The numerical results of Maragkos et al. [8] are also added.

The radial profiles of mean streamwise velocity at several downstream locations ($z = 0.2\,\mathrm{m}$, $0.4\,\mathrm{m}$ and $0.6\,\mathrm{m}$ above the inlet) are presented in Fig. 7.

Our simulation shows a satisfactory agreement with the experimental data and falls within the experimental uncertainties. The results are also inline with the numerical results [4, 8, 56]. We should mention that all the radial profiles are azimuthally averaged all around the plume.

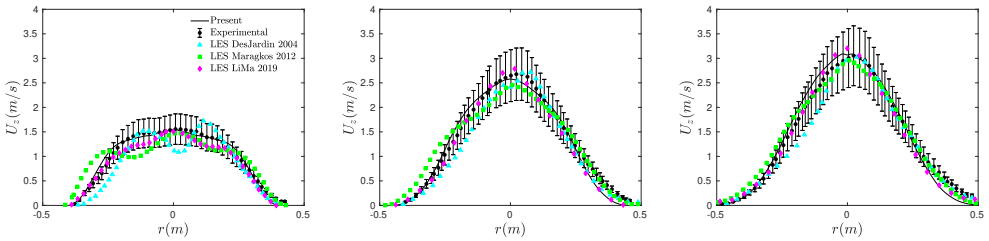

Figure 7: Comparison of mean radial profiles of streamwise velocity for different resolutions and different turbulence models at heights $z = 0.2\,\mathrm{m}$ (left), $z = 0.4\,\mathrm{m}$ (middle) and $z = 0.6\,\mathrm{m}$ (right). The experimental data includes the respective uncertainties reported in the experimental study [43]. Numerical data are also presented [4, 8, 56].

Figure 8 shows RMS values of the streamwise velocity at different heights. The results reproduce in overall well the experimental data. Nevertheless, at $z = 0.2\,\mathrm{m}$, the RMS profile exhibits an M-shaped profile, whereas the experimental profile is flatter. A similar behavior is observed by Maragkos *et* al. [8]. On the other hand, Desjardin *et* al. [4] overpredicted the centerline RMS values at all heights.

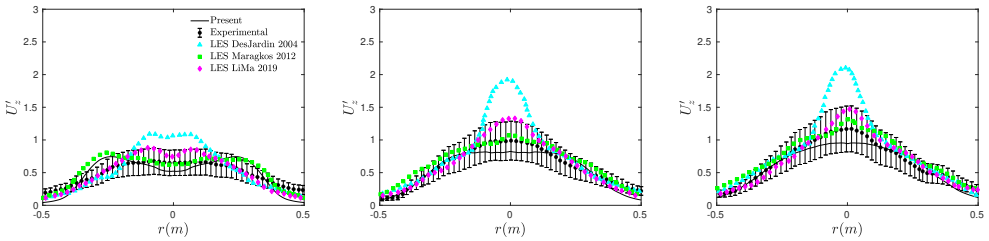

Figure 8: Comparison of rms radial profiles of streamwise velocity for different resolutions and different turbulence models at heights $z = 0.2\,\mathrm{m}$ (left), $z = 0.4\,\mathrm{m}$ (middle) and $z = 0.6\,\mathrm{m}$ (right). The experimental data includes the respective uncertainties reported in the experimental study [43]. Numerical data are also presented [4, 8, 56].

The cross-stream velocity is presented in Fig. 9. Our results show a good overall agreement with the experimental data. Maragkos *et* al. [8], DesJardin *et* al. [4] and Ma *et* al. [56] reported an overestimation on the left hand side of the plume as seen in Fig. 9. While keeping in mind that the

experimental data are not perfectly symmetric, we have the same behavior at $z = 0.2\,\mathrm{m}$ but the disparities in our results are lower. Afterwards farther downstream, the agreement becomes better compared to experimental data. The application of SGS model did not increase the cross-stream velocity as reported by Maragkos *et* al. [8].

A rise of the cross-stream velocity indicates an increased entrainment from the surrounding fluid which will result in a surge in the streamwise velocity following the conservation of mass. So accurate predictions of the cross-stream velocities is crucial, as in these type of flows, entertainment controls the mixing (as elaborated in a previous work [40]), which is a fundamental parameter in pool fires where the combustion process is mainly controlled by mixing (i.e., diffusion flame) as will be seen in Sec. 4.

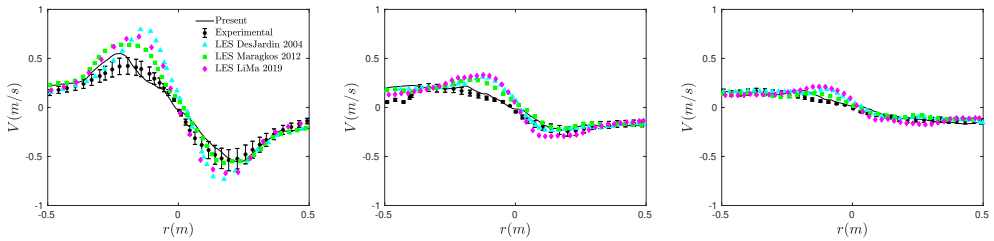

Figure 9: Comparison of mean radial profiles of cross-stream velocity for different resolutions and different turbulence models at heights $z = 0.2\,\mathrm{m}$ (left), $z = 0.4\,\mathrm{m}$ (middle) and $z = 0.6\,\mathrm{m}$ (right). The experimental data includes the respective uncertainties reported in the experimental study [43]. Numerical data are also presented [4, 8, 56].

Figure 10 shows the RMS values of the cross-stream velocity at different heights. The results agree with the experiment falling within the uncertainties except at some radial locations where they exhibit a slight overestimation. Our simulation shows an M-shaped for the RMS of the cross-stream velocities, coherent with the observations of Chung *et* al. [55], DesJardin *et* al. [4] and Maragkos *et* al. [8]. This M-shaped transits progressively to a bell-shaped profile as the height increases.

The radial profiles of mean helium mass fraction at different heights are presented in Fig. 11. Slight overestimation can be observed, especially at $z = 0.2\,\mathrm{m}$ at the left side of the plume. The discrepancies of the centerline value increase with height consistently with the overestimation in the axial profile seen in Fig. 6. The profiles align better with the experiment farther from the centerline. The LES of Maragkos *et* al. [8] is in better agreement in comparison with the experimental data.

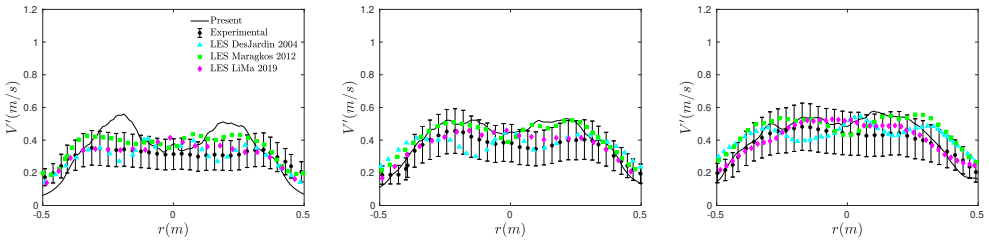

Figure 10: Comparison of rms radial profiles of cross-stream velocity for different resolutions and different turbulence models at heights $z = 0.2\,\mathrm{m}$ (left), $z = 0.4\,\mathrm{m}$ (middle) and $z = 0.6\,\mathrm{m}$ (right). The experimental data includes the respective uncertainties reported in the experimental study [43]. Numerical data are also presented [4, 8, 56].

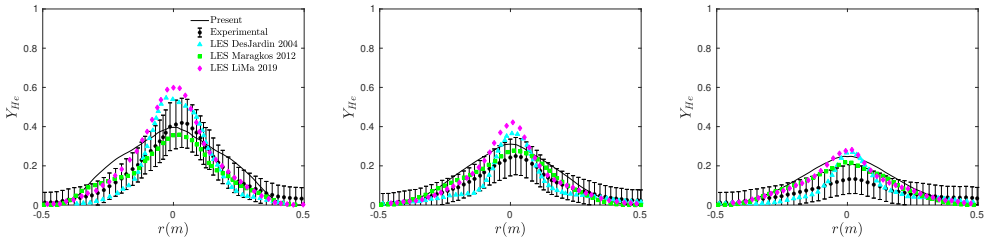

Figure 11: Comparison of mean radial profiles of helium's mass fraction for different resolutions and different turbulence models at heights $z = 0.2\,\mathrm{m}$ (left), $z = 0.4\,\mathrm{m}$ (middle) and $z = 0.6\,\mathrm{m}$ (right). The experimental data includes the respective uncertainties reported in the experimental study [43]. Numerical data are also presented [4, 8, 56].

Figure 12 shows the radial profiles of the RMS values of helium mass fraction. Globally, a significant over-prediction from the experimental data is observed close to the plume inlet for all the simulation. However, the discrepancies reduce farther downstream from the source. The results are consistent with those reported in previous numerical studies [4, 7, 56].

4. Sandia's 1-m diameter methane fire

4.1. Numerical Setup

The computational domain is a $4 \times 4 \times 7\,\mathrm{m}^3$ box, on which a non-uniform Cartesian grid was used with refinement zones for cost reduction. The largest and smallest mesh sizes in the computational domain are $\delta x_{max} = 4$ cm and $\delta x_{min} = 2$ cm, resulting in a 6-million cell mesh. The configuration of the 1 m diameter methane fire was simplified such that the fuel (methane) enters the domain through a 1 m diameter inlet surrounded by a 0.51 m wide steel plate (representing the ground plane).

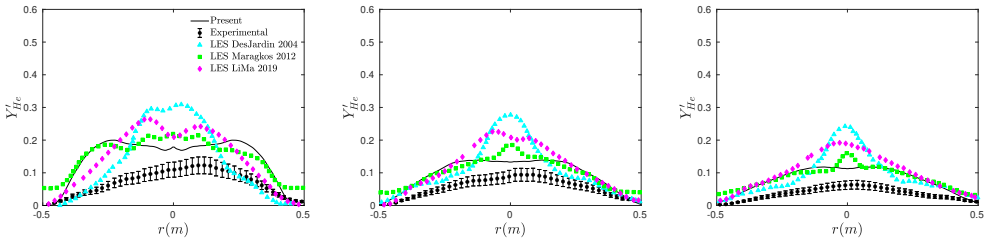

Figure 12: Comparison of rms radial profiles of helium's mass fraction for different resolutions and different turbulence models at heights $z = 0.2\,\mathrm{m}$ (left), $z = 0.4\,\mathrm{m}$ (middle) and $z = 0.6\,\mathrm{m}$ (right). The experimental data includes the respective uncertainties reported in the experimental study [43]. Numerical data are also presented [4, 8, 56].

Methane is injected at the ambient temperature and pressure, $\mathrm{T}_{inlet} = 285\,\mathrm{K}$ and $\mathrm{P}_{inlet} = 81.0\,\mathrm{kPa}$, respectively. Uniform bulk inlet velocity for methane is $U_{inlet}^{CH_4} = 0.097\,\mathrm{m/s}$ corresponding to TEST-24 conditions (see Table 1). In addition, a co-flow air stream is injected outside the annular plate with a uniform velocity of $U_{coflow}^{Air} = 0.14\,\mathrm{m/s}$. The value of the co-flow velocity was taken following the numerical studies of Han *et* al. [69] and Koo *et* al. [70]. Boundary conditions of the sides and the outlet are identical to the ones used in the helium study in Sec. 3. Velocities with negative values were forced to zero at the outlet to prevent flow rentering the domain (reverse flow), which might trigger numerical instabilities and pollute the results. The steel plate was modeled as an adiabatic non-slip wall.

A single-step irreversible chemical reaction of methane is considered:

$$\mathrm{CH_4} + 2(\mathrm{O_2} + 3.76\mathrm{N_2}) \rightarrow \mathrm{CO_2} + 2\mathrm{H_2O} + 7.52\mathrm{N_2} \tag{38}$$

The unresolved turbulent stress is modeled using the Vreman model (Sec. 2.2) with $C_s = 0.1$ [9]. In order to resolve the filtered heat and species fluxes, a value of 0.7 is assigned to both turbulent Prandtl (Pr_t) and Schmidt (Sc_t) numbers [9]. The molecular Prandtl number (Pr) is set to 0.7, while the molecular Schmidt numbers of the species are summarized in Table 3. The molecular viscosity follows a power law because the simulation will exhibit high levels of temperature due to combustion, which impacts the viscosity significantly. The radiant fraction is 25% of the total heat release.

The simulation is run over 27 physical seconds. The first 7 seconds are thought sufficient to evacuate the initial solution then the remaining 20 seconds are used to construct the statistics for quantitative comparisons. The time step is local and depends on the local mesh size while keeping a

CH_4	O_2	CO_2	H_2O
0.7275	0.8325	1.0425	0.6225

Table 3: Molecular Schmidt number Sc for different species

constant CFL number (CFL ≈ 0.7). This gives a minimum time step in the finest zone $\delta t_{min} \simeq 2.0 \times 10^{-4}$ sec. The simulation is parallelized on 128 cores on a Dell PowerEdge C6420 server with 4× 32-core Intel Xeon Gold 6142, 2.6 GHz, and 96 GB RAM producing a calculation time of $\sim$ 1050 CPU hours.

4.2. Results and discussion

4.2.1. Turbulence: Energy Cascade

Figure 13 shows the energy spectrum based on the axial velocity at $z = 0.5$ m. The spectrum exhibits the theoretical energy cascade characteristic reported by the theory of Kolmogorov [63] and that we have the correct power law of $-5/3$ in the inertial range, also the dissipation range was detected at higher frequencies.

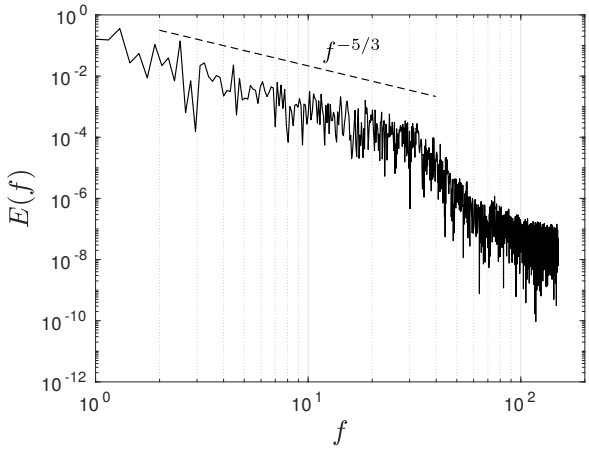

Figure 13: Temporal energy spectrum at $z = 0.5$ m for axial velocity. The dashed line indicates the expected characteristic slope of $-5/3$ [63].

4.2.2. Pool fire dynamics: Instability modes

Large-scale pool fires exhibit a particular behavior where a periodic shedding of large toroidal vortices pulsates at a specific frequency and is proportional to the square root of the diameter [22]. The "puffing" mechanism

is fundamental for fires as it controls the mixing between fuel and oxidizer, which conducts the combustion process. Figure 14 shows the different stages of a puffing cycle (four distinct stages); at first, instabilities are generated near the edges of the plume at the fire base due to baroclinic and gravitational torques; afterwards, those instabilities grow towards the center of the source; then, a large toroidal vortex is formed due to Rayleigh-Taylor instability which self-propagates and entrains a large amount of surrounding air; finally, the destruction of this toroidal vortex because of the creation of secondary instabilities and Kelvin-Helmholtz instabilities that grow causing a non-linear breakdown of the toroidal vortex. These stages are then repeated at every cycle, and the frequency of this motion was quantified experimentally, and numerical correlations were proposed.

Extensive experiments covering different scenarios and regimes of fires concluded that the puffing frequency depends only on the fire source diameter regardless of the fuel type. Correlations can be found in the literature that predicts the puffing frequency, such as the one given by Cetegen and Ahmed [22]:

$$f = 1.5\sqrt{D} \text{ Hz}, \tag{39}$$

and the one given by Zukoski [71]:

$$f = 0.5 \left(\frac{g}{D}\right)^{\frac{1}{2}} \text{ Hz} \tag{40}$$

Figure 15 shows the Fast Fourier transform (FFT) performed on the time signal of axial velocity at $z = 0.5\,\text{m}$ in order to identify the principal frequency of puffing. Our simulation predicts a puffing frequency of ~ 1.32 Hz which underestimates the experimental values of 1.57 Hz, while the correlation of Cetegen gives 1.5 Hz and the correlation of Zukoski estimates 1.57 Hz.

4.2.3. Mean and RMS profiles

The axial profiles of axial velocity and temperature are displayed in Fig. 16. The velocity U_z in the near-field region is in reasonable agreement with the experiment. On the other, comparisons with the McCaffrey correlations suggest that it is underestimated in the far-field region. The temperature decrease rate in the far field is consistent with the correlation of McCaffrey. However, the quantitative comparison suggests that the temperature is overestimated.

Figure 14: Snapshots of heat release rate iso-volume throughout 1 second depicting a complete puffing cycle.

Fig. 17 shows the radial profiles of axial velocity at different elevations downstream the inlet $z = 0.3, 0.5, 0.9\,\mathrm{m}$. A decent agreement can be observed with the experimental data, the predicted profiles remaining within the experimental uncertainties.

Fig. 18 depicts the radial profiles of horizontal velocity, which may be

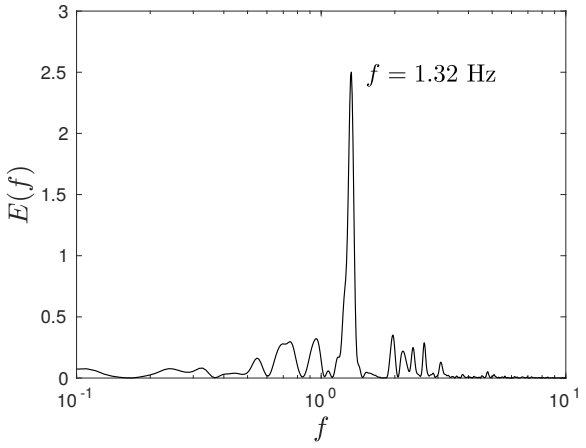

Figure 15: Fast Fourier transform (FFT) based on the axial velocity at $z = 0.5\,\mathrm{m}$ showing the puffing frequency.

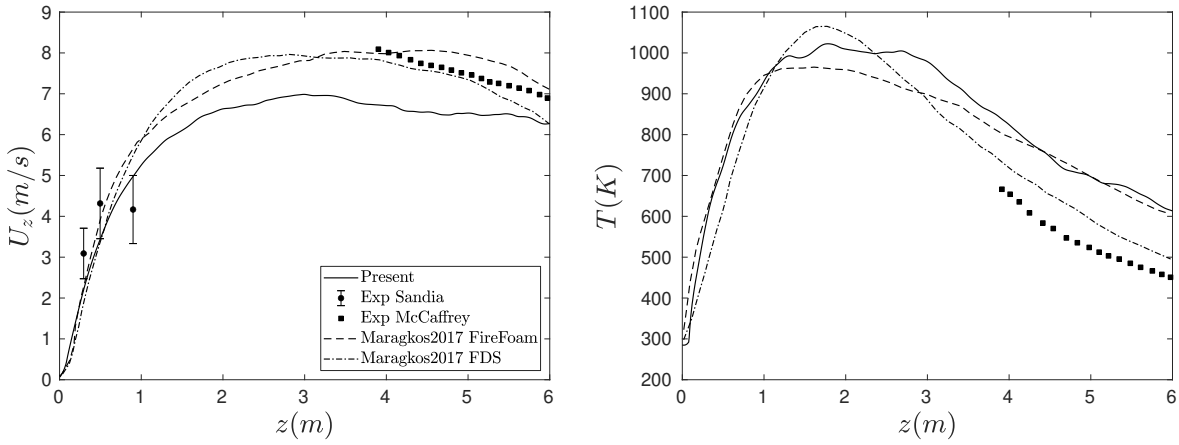

Figure 16: Centerline profiles of (left) mean streamwise velocity U_z and (right) temperature T compared to experimental and numerical data

considered as an indicator of the entrainment of air from the ambient environment toward the fire core. We can clearly notice a good agreement with the experimental and numerical data indicating a good prediction of the entrained air towards the fire core.

The rms of velocity was represented by the turbulent kinetic energy (TKE) which combines the three components of velocity fluctuations:

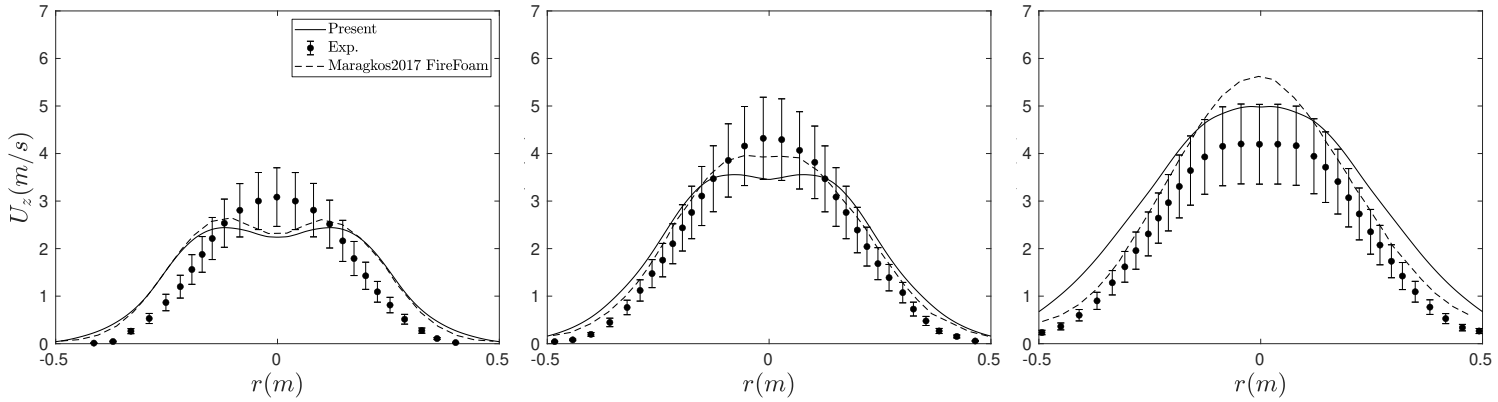

Figure 17: Radial profiles of streamwise velocity U_z at $z = 0.3\,\mathrm{m}$ (left), $z = 0.5\,\mathrm{m}$ (middle) and $z = 0.9\,\mathrm{m}$ (right). Comparison is done with experimental and numerical data [9, 45]

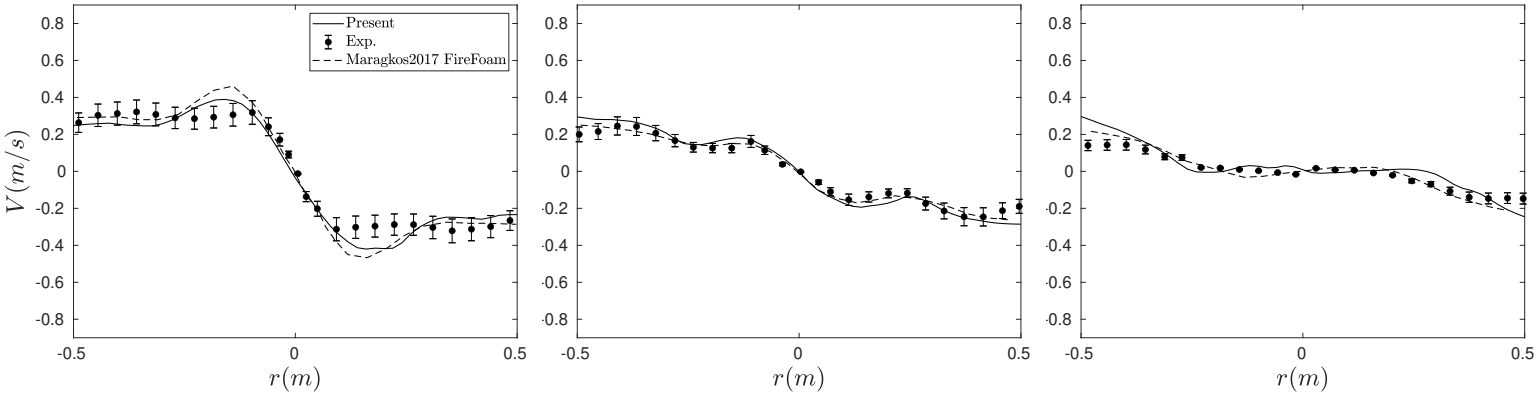

Figure 18: Radial profiles of horizontal velocity at $z = 0.3\,\mathrm{m}$ (left), $z = 0.5\,\mathrm{m}$ (middle) and $z = 0.9\,\mathrm{m}$ (right). Comparison is done with experimental and numerical data [9, 45]

$$\mathrm{TKE} = \frac{1}{2}\left(\overline{u_x'^2} + \overline{u_y'^2} + \overline{u_z'^2}\right) \tag{41}$$

Fig. 19 shows the turbulent kinetic energy at different heights. The agreement is reasonable, although noticeable discrepancies are observed further downstream the fire base (i.e., at $z = 0.9$ m).

4.2.4. Flame height

A quantitative criterion to define the average flame height is to identify the centerline location where the difference between the mean gas temper-

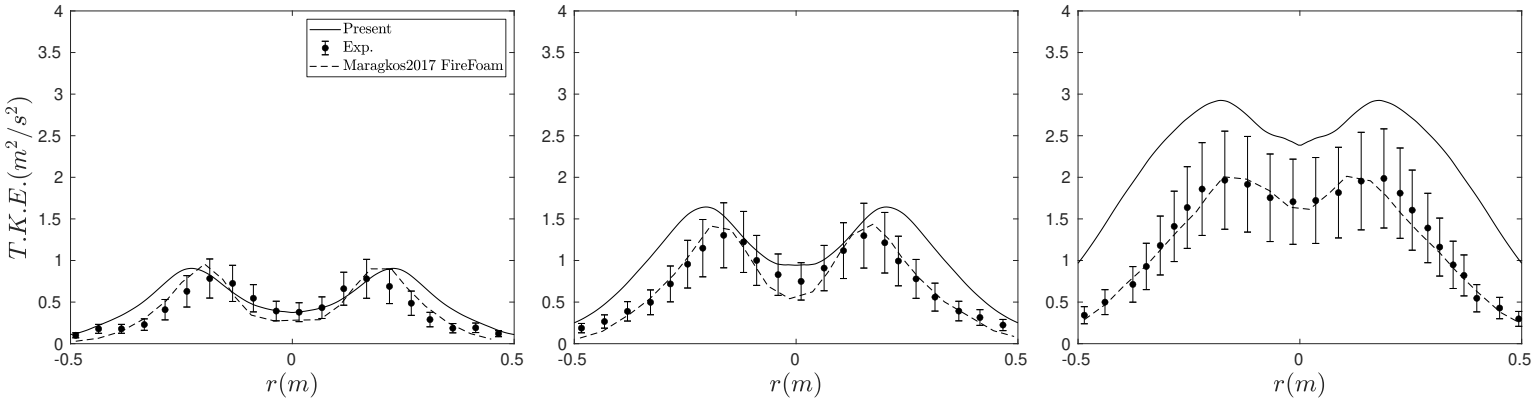

Figure 19: Radial profiles of turbulent kinetic energy (TKE) at $z = 0.3\,\mathrm{m}$ (left), $z = 0.5\,\mathrm{m}$ (middle) and $z = 0.9\,\mathrm{m}$ (right). Comparison is done with experimental and numerical data [9, 45]

ature and the ambient reaches 500 - 600 K [72]. In our study, a threshold of 550 K is selected following Maragkos and Merci [9]. Our LES estimates a height of 5.2 meters which is slightly higher than the reported value of 4.8 m [73].

5. Concluding remarks

LES of fire plume scenarios representative of unwanted fire were performed for the first time by using a pressure-based LBM solver with low-Mach number approximation. Two scenarios were selected involving large-scale helium and methane pool fires. The capability of the LBM-based LES to reproduce quantitatively the near-field dynamics of purely buoyant flows was clearly demonstrated, and numerical results were found similar to predictions reported with classical Navier-Stokes solvers at a lower computational cost. These results establish that LBM solvers are good candidates to serve as a basis for developing fire simulators. The next natural steps of this work will be to incorporate state-of-the-art turbulence and radiation sub-models to model more complex configurations.

Acknowledgments

Centre de Calcul Intensif d'Aix-Marseille and GENCI-TGCC/CINES (Grant 2022-A0132B11951) are acknowledged for granting access to their high-performance computing resources.

Data availability

The data that support the findings of this study are available from the corresponding author upon reasonable request.

References

[1] K. McGrattan, S. Hostikka, R. McDermott, J. Floyd, C. Weinschenk, K. Overholt, Dynamics simulator technical reference guide volume 1: Mathematical model, Tech. rep., NIST (2014).

[2] Firefoam, `http://code.google.-com/p/firefoam-dev/`.

[3] A. Brown, M. Bruns, M. Gollner, J. Hewson, G. Maragkos, A. Marshall, R. McDermott, B. Merci, T. Rogaume, S. Stoliarov, et al., Proceedings of the first workshop organized by the iafss working group on measurement and computation of fire phenomena (macfp), Fire safety journal 101 (2018) 1–17.

[4] P. E. DesJardin, T. J. O'Hern, S. R. Tieszen, Large eddy simulation and experimental measurements of the near-field of a large turbulent helium plume, Physics of fluids 16 (6) (2004) 1866–1883.

[5] P. E. Desjardin, Modeling of conditional dissipation rate for flamelet models with application to large eddy simulation of fire plumes, Combustion science and technology 177 (10) (2005) 1883–1916.

[6] S. Ferraris, J. Wen, S. Dembele, Large-eddy simulation of a large-scale methane pool fire, Fire Safety Science 8 (2005) 963–974.

[7] G. Maragkos, P. Rauwoens, B. Merci, Application of fds and firefoam in large eddy simulations of a turbulent buoyant helium plume, Combustion Science and Technology 184 (7-8) (2012) 1108–1120.

[8] G. Maragkos, P. Rauwoens, Y. Wang, B. Merci, Large eddy simulations of the flow in the near-field region of a turbulent buoyant helium plume, Flow, turbulence and combustion 90 (3) (2013) 511–543.

[9] G. Maragkos, B. Merci, Large eddy simulations of ch4 fire plumes, Flow, Turbulence and Combustion 99 (1) (2017) 239–278.

[10] G. Maragkos, B. Merci, Towards predictive simulations of gaseous pool fires, Proceedings of the Combustion Institute 37 (2019) 3927–3934.

[11] G. Maragkos, B. Merci, On the use of dynamic turbulence modelling in fire applications, Combustion and Flame 216 (2020) 9–23.

[12] M. M. Ahmed, A. Trouvé, Large eddy simulation of the unstable flame structure and gas-to-liquid thermal feedback in a medium-scale methanol pool fire, Combustion and Flame 225 (2021) 237–254.

[13] L. Ma, F. Nmira, J. Consalvi, Large eddy simulation of medium-scale methanol pool fires - effects of pool boundary conditions, Combustion and Flame 222 (2020) 336–354.

[14] L. Ma, F. Nmira, J. Consalvi, Exploring subgrid-scale variance models in les of lab-scale methane fire plumes, Combust. Theor. model. 25 (2021) 44–72.

[15] Y. Wang, P. Chatterjee, J. L. de Ris, Large eddy simulation of fire plumes, Proceedings of the Combustion Institute 33 (2) (2011) 2473–2480.

[16] Z. Chen, J. Wen, B. Xu, S. Dembele, Large eddy simulation of a medium-scale methanol pool fire using the extended eddy dissipation concept, Int. J. Heat Mass Transf. 70 (3) (2014) 389–408.

[17] P. Chatterjee, J. L. de Ris, Y. Wang, S. Dorofeev, A model for soot radiation in buoyant diffusion flames, Proc. Combust. Inst. 33 (2) (2011) 2665–2671.

[18] I. Sikic, S. Dembele, J. Wen, Non-grey radiative heat transfer modelling in les-cfd

simulated methanol pool fires, J. Quant. Spectrosc. Radiat. Transf. 234 (3) (2019) 78–89.

[19] F. Nmira, L. Ma, J. Consalvi, Influence of gas radiative property models on large eddy simulation of 1 m methanol pool fires, Combustion and Flame 221 (2020) 352–363.

[20] P. Chatterjee, J. L. de Ris, Y. Wang, S. Dorofeev, Application of a subgrid soot-radiation model in the numerical simulation of a heptane pool fire, Proc. Combust. Inst. 35 (3) (2015) 2573–2580.

[21] F. Nmira, A. Bouffard, J. Consalvi, Y. Wang, Large-eddy simulation of lab-scale ethylene buoyant diffusion flames: Effects of subgrid turbulence/soot production interaction and radiation models, Proc. Combust. Inst. 39 (2023) 1–10.

[22] B. M. Cetegen, T. A. Ahmed, Experiments on the periodic instability of buoyant plumes and pool fires, Combustion and flame 93 (1-2) (1993) 157–184.

[23] S. Tieszen, L. Gritzo, Transport phenomena that affect heat transfer in fully turbulent fires, in: B. Sunden, M. Faghri (Eds.), Transport Phenonema in Fires, WIT Press, Boston, 2008, Ch. 2, pp. 25–63.

[24] T. Krüger, H. Kusumaatmaja, A. Kuzmin, O. Shardt, G. Silva, E. M. Viggen, The lattice boltzmann method, Springer International Publishing 10 (978-3) (2017) 4–15.

[25] Y. Feng, P. Sagaut, W. Tao, A three dimensional lattice model for thermal compressible flow on standard lattices, Journal of Computational Physics 303 (2015) 514–529.

[26] Y. Feng, P. Sagaut, W.-Q. Tao, A compressible lattice boltzmann finite volume model for high subsonic and transonic flows on regular lattices, Computers & Fluids 131 (2016) 45–55.

[27] S. Guo, Y. Feng, J. Jacob, F. Renard, P. Sagaut, An efficient lattice boltzmann method for compressible aerodynamics on d3q19 lattice, Journal of Computational Physics (2020) 109570.

[28] G. Farag, S. Zhao, T. Coratger, P. Boivin, G. Chiavassa, P. Sagaut, A pressure-based regularized lattice-boltzmann method for the simulation of compressible flows, Physics of Fluids 32 (6) (2020) 066106.

[29] G. Farag, T. Coratger, G. Wissocq, S. Zhao, P. Boivin, P. Sagaut, A unified hybrid lattice-boltzmann method for compressible flows: bridging between pressure-based and density-based methods, Physics of Fluids 33 (8) (2021).

[30] T. Coratger, G. Farag, S. Zhao, P. Boivin, P. Sagaut, Large-eddy lattice-boltzmann modelling of transonic flows, Physics of Fluids 33 (11) (2021) 115112.

[31] Y. Feng, P. Boivin, J. Jacob, P. Sagaut, Hybrid recursive regularized thermal lattice boltzmann model for high subsonic compressible flows, Journal of Computational Physics 394 (2019) 82–99.

[32] I. Cheylan, S. Zhao, P. Boivin, P. Sagaut, Compressible pressure-based lattice-boltzmann applied to humid air with phase change, Applied Thermal Engineering (2021) 116868.

[33] J. Jacob, P. Sagaut, Wind comfort assessment by means of large eddy simulation with lattice boltzmann method in full scale city area, Building and Environment 139 (2018) 110–124.

[34] L. Merlier, J. Jacob, P. Sagaut, Lattice-boltzmann large-eddy simulation of pollutant dispersion in street canyons including tree planting effects, Atmospheric Environ-

ment 195 (2018) 89–103.
[35] L. Merlier, J. Jacob, P. Sagaut, Lattice-boltzmann large-eddy simulation of pollutant dispersion in complex urban environment with dense gas effect: Model evaluation and flow analysis, Building and Environment 148 (2019) 634–652.
[36] M. Tayyab, B. Radisson, C. Almarcha, B. Denet, P. Boivin, Experimental and numerical lattice-boltzmann investigation of the darrieus-landau instability, Combustion and Flame 221 (2020) 103–109.
[37] M. Tayyab, S. Zhao, Y. Feng, P. Boivin, Hybrid regularized lattice-boltzmann modelling of premixed and non-premixed combustion processes, Combustion and Flame 211 (2020) 173–184.
[38] M. Tayyab, S. Zhao, P. Boivin, Lattice-boltzmann modelling of a turbulent bluff-body stabilized flame, Physics of Fluids 33 (3) (2021) 031701.
[39] K. Bhairapurada, B. Denet, P. Boivin, A lattice-boltzmann study of premixed flames thermo-acoustic instabilities, Combustion and Flame 240 (2022) 112049.
[40] M. Taha, S. Zhao, A. Lamorlette, J.-L. Consalvi, P. Boivin, Lattice-boltzmann modeling of buoyancy-driven turbulent flows, Physics of Fluids 34 (5) (2022) 055131.
[41] G. Wang, S. Zhao, P. Boivin, E. Serre, P. Sagaut, A new hybrid lattice-boltzmann method for thermal flow simulations in low-mach number approximation, Physics of Fluids 34 (4) (2022) 046114.
[42] S. R. Tieszen, T. J. OHern, R. W. Schefer, L. Perea, Spatial and temporal resolution of fluid flows: Ldrd final report, Tech. rep., Sandia National Lab.(SNL-NM), Albuquerque, NM (United States) (1998).
[43] T. O'hern, E. Weckman, A. Gerhart, S. Tieszen, R. Schefer, Experimental study of a turbulent buoyant helium plume, Journal of Fluid Mechanics 544 (2005) 143–171.
[44] S. Tieszen, T. O'hern, R. Schefer, E. Weckman, T. Blanchat, Experimental study of the flow field in and around a one meter diameter methane fire, Combustion and Flame 129 (4) (2002) 378–391.
[45] S. Tieszen, T. O'hern, E. Weckman, R. Schefer, Experimental study of the effect of fuel mass flux on a 1-m-diameter methane fire and comparison with a hydrogen fire, Combustion and flame 139 (1-2) (2004) 126–141.
[46] T. Poinsot, D. Veynante, Theoretical and numerical combustion, RT Edwards, Inc., 2005.
[47] J. Smagorinsky, General circulation experiments with the primitive equations: I. the basic experiment, Monthly weather review 91 (3) (1963) 99–164.
[48] A. Vreman, An eddy-viscosity subgrid-scale model for turbulent shear flow: Algebraic theory and applications, Physics of fluids 16 (10) (2004) 3670–3681.
[49] K. McGrattan, S. Hostikka, R. McDermott, J. Floyd, C. Weinschenk, K. Overholt, Fire dynamics simulator user's guide, NIST special publication 1019 (6) (2013) 1–339.
[50] B. F. Magnussen, B. H. Hjertager, On mathematical modeling of turbulent combustion with special emphasis on soot formation and combustion, in: Symposium (international) on Combustion, Vol. 16, Elsevier, 1977, pp. 719–729.
[51] M. Yaga, H. Endo, T. Yamamoto, H. Aoki, T. Miura, Modeling of eddy characteristic time in les for calculating turbulent diffusion flame, International Journal of Heat and Mass Transfer 45 (11) (2002) 2343–2349.
[52] T. Krüger, H. Kusumaatmaja, A. Kuzmin, O. Shardt, G. Silva, E. M. Viggen, The

Lattice Boltzmann Method: Principles and Practice, Springer, 2016.
[53] G. Farag, S. Zhao, G. Chiavassa, P. Boivin, Consistency study of lattice-boltzmann schemes macroscopic limit, Physics of Fluids 33 (3) (2021) 031701.
[54] G. Wissocq, P. Sagaut, Hydrodynamic limits and numerical errors of isothermal lattice boltzmann schemes, Journal of Computational Physics 450 (2022) 110858.
[55] W. Chung, C. Devaud, Buoyancy-corrected k–ε models and large eddy simulation applied to a large axisymmetric helium plume, International journal for numerical methods in fluids 58 (1) (2008) 57–89.
[56] L. Ma, F. Nmira, J.-L. Consalvi, Verification and validation of a variable–density solver for fire safety applications, Numerical Heat Transfer, Part B: Fundamentals 76 (3) (2019) 107–129.
[57] E. Garnier, N. Adams, P. Sagaut, Large eddy simulation for compressible flows, Springer Science & Business Media, 2009.
[58] P. Boivin, M. Tayyab, S. Zhao, Benchmarking a lattice-boltzmann solver for reactive flows: Is the method worth the effort for combustion?, Physics of Fluids 33 (2021) 017703.
[59] A. Abdelsamie, G. Lartigue, C. E. Frouzakis, D. Thévenin, The taylor-green vortex as a benchmark for high-fidelity combustion simulations using low-mach solvers, Computers & Fluids 223 (2021) 104935.
[60] A. Suss, I. Mary, T. Le Garrec, S. Marié, Comprehensive comparison between the lattice boltzmann and navier–stokes methods for aerodynamic and aeroacoustic applications, Computers & Fluids 257 (2023) 105881.
[61] S. Zhao, K. Bhairapurada, M. Tayyab, R. Mercier, P. Boivin, Lattice-boltzmann modelling of the quiet and unstable preccinsta burner modes, Computers and Fluids 260 (2023) 105898.
[62] J. Latt, C. Coreixas, J. Beny, Cross-platform programming model for many-core lattice boltzmann simulations, Plos one 16 (4) (2021) e0250306.
[63] A. N. Kolmogorov, The local structure of turbulence in incompressible viscous fluid for very large reynolds numbers, Cr Acad. Sci. URSS 30 (1941) 301–305.
[64] X. Jiang, K. Luo, Spatial direct numerical simulation of the large vortical structures in forced plumes, Flow, turbulence and combustion 64 (1) (2000) 43–69.
[65] X. Jiang, K. H. Luo, Spatial dns of flow transition of a rectangular buoyant reacting free-jet, Journal of Turbulence 2 (1) (2001) 015.
[66] X. Jiang, K. Luo, Dynamics and structure of transitional buoyant jet diffusion flames with side-wall effects, Combustion and flame 133 (1-2) (2003) 29–45.
[67] E. Weckman, A. Sobiesiak, The oscillatory behaviour of medium-scale pool fires, in: Symposium (International) on Combustion, Vol. 22, Elsevier, 1989, pp. 1299–1310.
[68] B. M. Cetegen, K. D. Kasper, Experiments on the oscillatory behavior of buoyant plumes of helium and helium-air mixtures, Physics of fluids 8 (11) (1996) 2974–2984.
[69] W. Han, J. Lin, G. H. Yeoh, E. R. Hawkes, Les/pdf modelling of a one-meter diameter methane fire plume, Proceedings of the Combustion Institute 38 (3) (2021) 4943–4951.
[70] H. Koo, R. C. Knaus, J. C. Hewson, S. P. Domino, Model sensitivities in les predictions of buoyant methane fire plumes., Tech. rep., Sandia National Lab.(SNL-NM), Albuquerque, NM (United States) (2017).
[71] E. Zukoski, Properties of fire plumes, Academic Press, 1995.

[72] D. Drysdale, An introduction to fire dynamics, John Wiley & Sons, 2011.
[73] G. Marjanovic, G. Taub, S. Balachandar, On the evolution of the plume function and entrainment in the near-source region of lazy plumes, Journal of Fluid Mechanics 830 (2017) 736–759.

Appendix A. Expressions for the LBM solver

In regularized LBM, distribution functions will be constructed using an orthogonal polynomial basis. The basis of the D3Q19r lattice used in the current study consists of 19 polynomials, read [29]

$$\mathcal{H}_{i}^{(0)} \equiv 1 \ , \quad \mathcal{H}_{i,\alpha}^{(1)} \equiv c_{i\alpha} \ , \quad \mathcal{H}_{i,\alpha\beta}^{(2)} \equiv c_{i\alpha}c_{i\beta} - c_s^2\delta_{\alpha\beta}, \tag{A.1}$$

$$\mathcal{H}_{i,1}^{(3r)} \equiv \mathcal{H}_{i,xxy}^{(3)} + \mathcal{H}_{i,yzz}^{(3)}, \tag{A.2}$$

$$\mathcal{H}_{i,2}^{(3r)} \equiv \mathcal{H}_{i,xzz}^{(3)} + \mathcal{H}_{i,xyy}^{(3)}, \tag{A.3}$$

$$\mathcal{H}_{i,3}^{(3r)} \equiv \mathcal{H}_{i,yyz}^{(3)} + \mathcal{H}_{i,xxz}^{(3)}, \tag{A.4}$$

$$\mathcal{H}_{i,4}^{(3r)} \equiv \mathcal{H}_{i,xxy}^{(3)} - \mathcal{H}_{i,yzz}^{(3)}, \tag{A.5}$$

$$\mathcal{H}_{i,5}^{(3r)} \equiv \mathcal{H}_{i,xzz}^{(3)} - \mathcal{H}_{i,xyy}^{(3)}, \tag{A.6}$$

$$\mathcal{H}_{i,6}^{(3r)} \equiv \mathcal{H}_{i,yyz}^{(3)} - \mathcal{H}_{i,xxz}^{(3)}, \tag{A.7}$$

$$\mathcal{H}_{i,1}^{(4r)} \equiv \frac{4}{9}\left(3+2\sqrt{3}\right)\mathcal{D}_{i,xyz}^{(4)} + \frac{4}{9}\left(3-\sqrt{3}\right)\mathcal{D}_{i,xzy}^{(4)} + \frac{4}{9}\left(3-\sqrt{3}\right)\mathcal{D}_{i,zyx}^{(4)} \, , \tag{A.8}$$

$$\mathcal{H}_{i,2}^{(4r)} \equiv \frac{4}{9}\left(3+2\sqrt{3}\right)\mathcal{D}_{i,xzy}^{(4)} + \frac{4}{9}\left(3-\sqrt{3}\right)\mathcal{D}_{i,xyz}^{(4)} + \frac{4}{9}\left(3-\sqrt{3}\right)\mathcal{D}_{i,zyx}^{(4)} \, , \tag{A.9}$$

$$\mathcal{H}_{i,3}^{(4r)} \equiv \frac{4}{9}\left(3+2\sqrt{3}\right)\mathcal{D}_{i,zyx}^{(4)} + \frac{4}{9}\left(3-\sqrt{3}\right)\mathcal{D}_{i,xzy}^{(4)} + \frac{4}{9}\left(3-\sqrt{3}\right)\mathcal{D}_{i,xyz}^{(4)} \, , \tag{A.10}$$

where

$$\mathcal{H}_{i,\alpha\beta\gamma}^{(3)} \equiv c_{i\alpha}c_{i\beta}c_{i\gamma} - c_s^2[c_{i\alpha}\delta_{\beta\gamma} + c_{i\beta}\delta_{\gamma\alpha} + c_{i\gamma}\delta_{\alpha\beta}] \ , \tag{A.11}$$

$$\mathcal{D}_{i,\alpha\beta\gamma}^{(4)} \equiv \mathcal{H}_{i,\alpha\alpha\beta\beta}^{(4)} + \frac{c_s^2}{2}\mathcal{H}_{i,\gamma\gamma}^{(2)} \ , \tag{A.12}$$

$$\begin{aligned}\mathcal{H}_{i,\alpha\beta\gamma\delta}^{(4)} \equiv & c_{i\alpha}c_{i\beta}c_{i\gamma}c_{i\delta} + c_s^4(\delta_{\alpha\beta}\delta_{\gamma\delta} + \delta_{\beta\gamma}\delta_{\delta\alpha} + \delta_{\delta\alpha}\delta_{\beta\gamma}) \\ & - c_s^2(c_{i\alpha}c_{i\beta}\delta_{\gamma\delta} + c_{i\beta}c_{i\gamma}\delta_{\delta\alpha} + c_{i\gamma}c_{i\delta}\delta_{\alpha\beta} + c_{i\delta}c_{i\alpha}\delta_{\beta\gamma} + c_{i\gamma}c_{i\alpha}\delta_{\beta\delta} + c_{i\beta}c_{i\delta}\delta_{\alpha\gamma}) \, .\end{aligned} \tag{A.13}$$

Any distribution function in the D3Q19r lattice can be written as a (weighted) sum of the contributions from each base polynomial. For in-

stance, the equilibrium distribution in equation (28) reads

$$f_i^{\mathrm{eq},19r} = \omega_i \left\{ a^{(0),\mathrm{eq}} + \frac{\mathcal{H}^{(1)}_{i,\alpha}}{c_s^2} a^{(1),\mathrm{eq}}_{\alpha} + \frac{\mathcal{H}^{(2)}_{i,\alpha\beta}}{2c_s^4} a^{(2),\mathrm{eq}}_{\alpha\beta} + \frac{\mathcal{H}^{(3r)}_{i,\gamma}}{6c_s^6} a^{(3r),\mathrm{eq}}_{\gamma} + \frac{\mathcal{H}^{(4r)}_{i,\delta}}{24c_s^8} a^{(4r),\mathrm{eq}}_{\delta} \right\} , \tag{A.14}$$

where

$$a^{(0),\mathrm{eq}} = \rho\theta \ , \quad a^{(1),\mathrm{eq}}_{\alpha} = \rho u_{\alpha} \ , \quad a^{(2),\mathrm{eq}}_{\alpha\beta} = \rho u_{\alpha} u_{\beta} \tag{A.15}$$

$$a_1^{(3r),\mathrm{eq}} = 3(\rho u_x u_x u_y + \rho u_y u_z u_z) \ , \tag{A.16}$$

$$a_2^{(3r),\mathrm{eq}} = 3(\rho u_x u_z u_z + \rho u_x u_y u_y) \ , \tag{A.17}$$

$$a_3^{(3r),\mathrm{eq}} = 3(\rho u_y u_y u_z + \rho u_x u_x u_z) \ , \tag{A.18}$$

$$a_4^{(3r),\mathrm{eq}} = \rho u_x u_x u_y - \rho u_y u_z u_z \ , \tag{A.19}$$

$$a_5^{(3r),\mathrm{eq}} = \rho u_x u_z u_z - \rho u_x u_y u_y \ , \tag{A.20}$$

$$a_6^{(3r),\mathrm{eq}} = \rho u_y u_y u_z - \rho u_x u_x u_z \ , \tag{A.21}$$

$$a_1^{(4r),\mathrm{eq}} = -\rho c_s^2 \left[\frac{-4\sqrt{3}-6}{9} u_z^2 + \frac{2\sqrt{3}-6}{9} \left(u_x^2 + u_y^2 \right) \right] , \tag{A.22}$$

$$a_2^{(4r),\mathrm{eq}} = -\rho c_s^2 \left[\frac{-4\sqrt{3}-6}{9} u_y^2 + \frac{2\sqrt{3}-6}{9} \left(u_x^2 + u_z^2 \right) \right] , \tag{A.23}$$

$$a_3^{(4r),\mathrm{eq}} = -\rho c_s^2 \left[\frac{-4\sqrt{3}-6}{9} u_x^2 + \frac{2\sqrt{3}-6}{9} \left(u_y^2 + u_z^2 \right) \right] . \tag{A.24}$$

It is worth noting that the the forth-order coefficients ($a^{(4),\mathrm{eq}}$) are added to improve the isotropicity of the lattice, which could be quite important considering the round jet simulation in the current study.

The third-order off-equilibrium terms are reconstructed recursively from

the second-order non-equilibrium tensor as

$$\begin{aligned}
a^{(3),\mathrm{neq}}_{\alpha\beta\gamma} &= u_\alpha a^{(2),\mathrm{neq}}_{\beta\gamma} + u_\beta a^{(2),\mathrm{neq}}_{\alpha\gamma} + u_\gamma a^{(2),\mathrm{neq}}_{\alpha\beta} \\
a^{(3r),\mathrm{neq}}_{1} &\equiv a^{(3),\mathrm{neq}}_{xxy} + a^{(3),\mathrm{neq}}_{yzz} \\
a^{(3r),\mathrm{neq}}_{2} &\equiv a^{(3),\mathrm{neq}}_{xzz} + a^{(3),\mathrm{neq}}_{xyy} \\
a^{(3r),\mathrm{neq}}_{3} &\equiv a^{(3),\mathrm{neq}}_{yyz} + a^{(3),\mathrm{neq}}_{xxz} \\
a^{(3r),\mathrm{neq}}_{4} &\equiv a^{(3),\mathrm{neq}}_{xxy} - a^{(3),\mathrm{neq}}_{yzz} \\
a^{(3r),\mathrm{neq}}_{5} &\equiv a^{(3),\mathrm{neq}}_{xzz} - a^{(3),\mathrm{neq}}_{xyy} \\
a^{(3r),\mathrm{neq}}_{6} &\equiv a^{(3),\mathrm{neq}}_{yyz} - a^{(3),\mathrm{neq}}_{xxz}
\end{aligned} \tag{A.25}$$

Depending on the order of the Gauss-Hermite quadrature [24] used in the LB model, an adequate forcing term should be added to achieve a correct viscous stress tensor:

$$a^{\mathrm{neq}}_{\alpha\beta} \approx -\Pi_{\alpha\beta} = -\mu(\frac{\partial u_\alpha}{\partial x_\beta} + \frac{\partial u_\beta}{\partial x_\alpha} - \frac{2}{D}\frac{\partial u_\gamma}{\partial x_\gamma}\delta_{\alpha\beta}), \tag{A.26}$$

with D the spatial dimension. For the D3Q19r basis, the projected forcing term reads as

$$a^{F^E}_{\alpha\beta} = c_s^2 u_\alpha \left[\frac{\partial(\rho(1-\theta))}{\partial x_\beta}\right] + c_s^2 u_\beta \left[\frac{\partial(\rho(1-\theta))}{\partial x_\alpha}\right] + \delta_{\alpha\beta}\rho c_s^2 \frac{2}{D}\frac{\partial u_\gamma}{\partial x_\gamma} - a^{\mathrm{cor}}_{\alpha\beta} - a^{F_D}_{\alpha\beta} \tag{A.27}$$

where $a^{\mathrm{cor}}_{\alpha\beta}$ is a correction tensor due to the deflection of second order moments of the population introduced by the modification of the mass equation, which can be evaluated as

$$a^{\mathrm{cor}}_{\alpha\beta} \equiv c_s^2 \delta_{\alpha\beta} \frac{\partial(\rho(1-\theta))}{\partial t}, \tag{A.28}$$

which can be discretized using a backward Euler operator and $a^{F_D}_{\alpha\beta}$ the correction tensor due to the defect of the lattice at third order

$$a^{F_D}_{\alpha\beta} = -\begin{pmatrix} (\rho u_x^3)_{,x} & (\rho u_x u_y u_z)_{,z} & (\rho u_x u_y u_z)_{,y} \\ (\rho u_x u_y u_z)_{,z} & (\rho u_y^3)_{,y} & (\rho u_x u_y u_z)_{,x} \\ (\rho u_x u_y u_z)_{,y} & (\rho u_x u_y u_z)_{,x} & (\rho u_z^3)_{,z} \end{pmatrix} \tag{A.29}$$

where all the differential operations are performed using first order upwind FD except for the divergence operator for which a second order centered FD scheme was employed. The final expression of the forcing term is then

$$F^E_i = \frac{\omega_i}{2c_s^4}\mathcal{H}^{(2)}_{i,\alpha\beta} a^{F^E}_{\alpha\beta} + F^g_i, \tag{A.30}$$

where F_i^g is the gravity force term defined as

$$F_i^g = \omega_i(\rho - \rho_\infty)\left[\frac{g_\alpha \mathcal{H}_{i,\alpha}^{(1)}}{c_s^2} + \frac{(u_\alpha g_\beta + u_\beta g_\alpha)\mathcal{H}_{i,\alpha\beta}^{(2)}}{2c_s^4}\right], \tag{A.31}$$

where g_α is the gravity acceleration in the direction α.

Appendix B. Vorticity equation

Helmholtz equation is the transport equation for vorticity, which can be deduced as follows. Starting from writing the momentum equation of incompressible flow, that is $\nabla \cdot \mathbf{u} = 0$, but with a variable density ρ.

$$\frac{\partial \mathbf{u}}{\partial t} + \mathbf{u} \cdot \nabla \mathbf{u} = -\frac{1}{\rho}\nabla p + \frac{1}{\rho}\nabla \cdot \tau + \frac{(\rho - \rho_\infty)}{\rho}\mathbf{g}, \tag{B.1}$$

The convective term $\mathbf{u} \cdot \nabla \mathbf{u}$ can be written in the following form:

$$\mathbf{u} \cdot \nabla \mathbf{u} = \nabla(\mathbf{u}^2/2) + \boldsymbol{\omega} \times \mathbf{u}, \tag{B.2}$$

The following vector identity will be used:

$$\nabla \times (\boldsymbol{\omega} \times \mathbf{u}) = (\mathbf{u} \cdot \nabla)\boldsymbol{\omega} - \underbrace{\mathbf{u}(\nabla \cdot \boldsymbol{\omega})}_{zero} - (\boldsymbol{\omega} \cdot \nabla)\mathbf{u} + \boldsymbol{\omega}(\nabla \cdot \mathbf{u}), \tag{B.3}$$

where $\nabla \cdot \boldsymbol{\omega} \equiv 0$ (vorticity is solenoidal by definition), the vorticity equation can be rearranged as:

$$\underbrace{\frac{\partial \boldsymbol{\omega}}{\partial t} + (\mathbf{u} \cdot \nabla)\boldsymbol{\omega}}_{D\boldsymbol{\omega}/Dt} = (\boldsymbol{\omega} \cdot \nabla)\mathbf{u} - \boldsymbol{\omega}(\nabla \cdot \mathbf{u}) - \nabla \times \left(\frac{1}{\rho}\nabla p\right) + \nabla \times \left(\frac{1}{\rho}\nabla \cdot \tau\right) + \nabla \times \left[(1 - \frac{\rho_\infty}{\rho})\mathbf{g}\right], \tag{B.4}$$

The pressure term can be written as:

$$\nabla \times \left(\frac{1}{\rho}\nabla p\right) = \nabla\left(\frac{1}{\rho}\right) \times \nabla p + \underbrace{\frac{1}{\rho}\nabla \times (\nabla p)}_{\text{zero}} = -\frac{1}{\rho^2}\left(\nabla\rho \times \nabla p\right), \tag{B.5}$$

Further more for a **homentropic** flow, the pressure is a function of only of density resulting in the alignment of the two vector ∇p and $\nabla \rho$ and consequently the so called baroclinic torque $-\left(\nabla\rho \times \nabla p\right)/\rho^2$ will vanish. By the same manner, the buoyancy term will be treated:

$$\nabla\times\left[(1-\frac{\rho_\infty}{\rho})\mathbf{g}\right]=\underbrace{\nabla\times\mathbf{g}}_{\text{zero}}-\nabla\times\left(\frac{\rho_\infty}{\rho}\mathbf{g}\right)=-\nabla\left(\frac{\rho_\infty}{\rho}\right)\times\mathbf{g}-\underbrace{\frac{\rho_\infty}{\rho}(\nabla\times\mathbf{g})}_{\text{zero}}=\frac{\rho_\infty}{\rho^2}(\nabla\rho\times\mathbf{g}), \tag{B.6}$$

By introducing the material derivative of the vorticity, $D\boldsymbol{\omega}/Dt$, the vorticity equation yields to:

$$\frac{D\boldsymbol{\omega}}{Dt}=\underbrace{(\boldsymbol{\omega}\cdot\nabla)\boldsymbol{u}}_{\text{vortex stretching}}-\underbrace{\boldsymbol{\omega}(\nabla\cdot\boldsymbol{u})}_{\text{vortex dilatation}}+\underbrace{\frac{1}{\rho^2}(\nabla\rho\times\nabla p)}_{\text{baroclinic torque}}+\underbrace{\frac{\rho_\infty}{\rho^2}(\nabla\rho\times\mathbf{g})}_{\text{gravitational torque}}+\underbrace{\nabla\times\left(\frac{1}{\rho}\nabla\cdot\tau\right)}_{\text{viscous diffusion}}. \tag{B.7}$$